The path toward vertical grid options for the Community Atmosphere Model version 7: the impact of vertical resolution on the QBO and tropical waves

Isla R. Simpson[1], Rolando R. Garcia[1], Julio T. Bacmeister[1], Peter H. Lauritzen[1], Cecile Hannay[1], Brian Medeiros[1], Julie Caron[1], Gokhan Danabasoglu[1], Adam Herrington[1], Christiane Jablonowski[2], Dan Marsh[1,3], Richard B. Neale[1], Lorenzo M. Polvani[4,5], Jadwiga H. Richter[1], Nan Rosenbloom[1], Simone Tilmes[2]

[1]NSF National Center for Atmospheric Research, Boulder, CO, USA
[2]Department of Climate and Space Sciences and Engineering, University of Michigan, Ann Arbor, MI, USA
[3]School of Physics and Astronomy, University of Leeds, Leeds, UK
[4]Department of Applied Physics and Applied Mathematics, Columbia University, New York, NY, USA
[5]Lamont-Doherty Earth Observatory, Columbia University, Palisades, NY, USA

Key Points:

- Resolved wave-driving of the quasi-biennial oscillation increases with vertical resolution.
- A 93-level mid-top (∼80-km top) and a 58-level low-top (∼40-km top) grid are proposed for the next generation Community Atmosphere Model.
- Despite an improved quasi-biennial oscillation in the mid-top, its observed connection with the Madden-Julian Oscillation is not reproduced.

Corresponding author: Isla Simpson, `islas@ucar.edu`

Abstract

The Community Earth System Model currently contains two primary atmospheric configurations: the Community Atmosphere Model 6 (CAM6, 32 levels, ∼40-km top); and the Whole Atmosphere Community Climate Model 6 (WACCM6, 70 levels, ∼140-km top). For CAM7, a number of factors motivate a raising of the model top and enhancement of the vertical resolution and this study documents the decision making process toward this next generation vertical grid. As vertical resolution in the troposphere/lower stratosphere is increased, the role of the resolved waves in driving the Quasi-Biennial Oscillation (QBO) is enhanced, becoming more aligned with ERA5 reanalysis. This can be traced to improved equatorial Kelvin waves and their vertical momentum fluxes. It is further shown that a model lid at ∼80-km does not have detrimental impacts on the representation of the QBO compared to a 140-km top. Based on this analysis, the vertical grid for CAM7 will have an ∼80-km top with 93 levels, 500-m grid spacing in the troposphere and lower stratosphere, and 10 additional levels in the boundary layer compared to CAM6. A 58-level/∼40-km low-top option will also be available. We further introduce new coupled simulations using CAM6 but with with CAM7's vertical grid above the boundary layer and used these to demonstrate that basic features of the stratospheric circulation are similar to WACCM6, despite the lower model top. They further show that despite the higher fidelity of the QBO, the observed connection between the QBO and the Madden-Julian Oscillation is absent.

Plain Language Summary

This study explores the impacts of changing the vertical grid spacing and model lid height on the representation of the atmosphere within the Community Atmosphere Model (CAM) to inform decisions regarding the vertical grid choices for the next generation of this model (CAM7). It is shown that decreasing the grid spacing (increasing the resolution) in the troposphere and lower stratosphere can lead to a better representation of tropical waves and their role in driving the Quasi-Biennial Oscillation (QBO) - a quasi-periodic variation in the winds of the lower stratosphere. It is also shown that a viable representation of the stratospheric polar vortices and the QBO can be obtained with a model lid placed at approximately 80 km. Overall, this analysis motivates the decisions made with regards to the grid for CAM7 and a suite of simulations that use this new grid are described. These simulations are then assessed for their representation of the observed connection between the QBO and the Madden-Julian Oscillation (MJO) - a mode of variability in the tropical troposphere. Despite the high fidelity of the QBO in this model, the QBO-MJO connection remains absent.

1 Introduction

Earth System Models (ESMs) are numerical representations of the coupled Earth system that are used to study the fundamental processes involved in the Earth's climate and to provide predictions for how the climate will evolve on timescales ranging from weeks to centuries. Model developers continue to strive to improve the representation of the processes relevant to the climate system under the constraint of available computing resources. The Community Earth System Model (CESM) is one such ESM (Hurrell et al., 2013; Danabasoglu et al., 2020). CESM is developed by the National Science Foundation National Center for Atmospheric Research in collaboration with other researchers. The model is open source, extensively documented, and well supported and, as a result, is used by many researchers around the world for a wide variety of applications. As part of the continued drive toward improved atmospheric representation within CESM, the next generation of one of CESM's atmospheric components (the Community Atmosphere Model version 7, CAM7) will have enhanced vertical resolution throughout the troposphere and stratosphere as well as a raised model lid compared to its predecessor, CAM6.

Here, we document the decision making process that led to this new vertical grid, while also demonstrating the dependencies of the representation of the atmosphere on vertical resolution in CESM. We also introduce some new simulations that are available to the broader research community to explore the impacts of this enhanced vertical resolution on climate variability and change within CESM.

CESM offers two primary atmospheric configurations: CAM and the Whole Atmosphere Community Climate Model (WACCM). WACCM is a high-top configuration and is typically run with fully interactive chemistry but can also be run in a specified chemistry mode (SC-WACCM) (Smith et al., 2014). It has been used for middle atmosphere studies where a good representation of stratospheric and mesospheric processes is key. The most recent version, WACCM6 (Gettelman et al., 2019), has a model lid at almost 140 km with 70 levels in the vertical. WACCM is built on top of the low-top model CAM. CAM has a model lid at around 40 km and CAM6 has 32 levels in the vertical and does not contain the same comprehensive representation of stratospheric chemistry as WACCM. Given its reduced computational expense relative to WACCM, CAM has been the "workhorse" model for many applications including contributions to the Coupled Model Intercomparison Projects (CMIP, (Eyring et al., 2016)) and large ensembles (Kay et al., 2014; Rodgers et al., 2021). Now, moving toward the development of version 3 of CESM (CESM3), the following factors have motivated an enhancement of the vertical resolution of CAM:

- It is now well established that the stratosphere has an impact on the troposphere (Baldwin & Dunkerton, 2001; Shaw & Shepherd, 2008; Anstey & Shepherd, 2014; Hitchcock & Simpson, 2014; Domeisen et al., 2020) and, with a model lid at $\sim$40 km, CAM's capacity to represent stratospheric processes is limited.
- There is a need to represent the Quasi-Biennial Oscillation (QBO) (Baldwin et al., 2001) given its potential as a source of predictability on seasonal to interannual timescales through, for example, recently identified connections with the Madden-Julian Oscillation (MJO) (Yoo & Son, 2016). While WACCM does produce an internally generated QBO, the vertical grid spacing is still too coarse to sufficiently represent the amplitude of the QBO in the lower stratosphere (Richter et al., 2020) and higher vertical resolution is needed to achieve this (Garcia & Richter, 2019).
- CESM is increasingly being used for sub-seasonal to seasonal prediction (e.g., Richter et al., 2022; Yeager et al., 2022) and, given that stratospheric variability is a potential source of predictability on these timescales (Domeisen et al., 2020), it is desirable to use a model with a well resolved stratosphere for these efforts. While WACCM does represent the stratosphere well, aside from the aforementioned issues regarding the QBO, the model lid at $\sim$140 km makes it challenging to initialize using existing reanalysis products from other systems, as is commonly done for prediction efforts with CESM. The optimum from an initialized prediction standpoint would, therefore, be a model that resolves the stratosphere well, but with a lid that still allows it to be initialized from reanalysis products, such as ERA5 (Hersbach et al., 2020), i.e., a model lid around 80 km.
- CESM is increasingly being used for applications with higher horizontal resolution either globally, or with regional refinement, so enhanced vertical resolution would likely be beneficial as the horizontal resolution is increased.
- There are motivations to enhance the resolution in the boundary layer as well, although this is not the focus of the present study. These motivations include adding the ability to capture thin cloud layers to improve the representation of stratocumulus clouds (Bogenschutz et al., 2023), improving the representation of thin, stable boundary layers (Byrkjedal et al., 2008), and also to lower the lowest model level to a location where the Monin-Obhukov similarity theory is a more valid approximation (Jiang & Hu, 2023).

The above factors motivate the exploration of a new vertical grid for CAM, one that has a model lid within the realm of existing reanalysis products (i.e., ∼80 km) but with sufficient vertical resolution in the troposphere and lower stratosphere to improve the representation of the QBO over the existing WACCM grid, as well as with enhancements of resolution within the boundary layer and with a lowering of the lowest model level.

In the following, we present a systematic assessment of the impacts of vertical resolution in the free troposphere and lower stratosphere with a primary focus on the QBO and other features of the tropical atmosphere given that these are likely to be most impacted by these changes in the vertical grid. The representation of the tropical stratosphere and its variability motivates the final choice of vertical grid for CAM7 and we then present some new simulations that use this grid above the boundary layer and with an ∼80 km model lid. These simulations are used to verify that this grid with a lid at around 80 km does not substantially degrade the representation of the stratospheric polar vortices compared to existing WACCM simulations and they are used to assess this model configuration, which now represents the QBO well, for the connection between the QBO and the MJO that has been found in observations.

We stress that all the analyses presented here are carried out with the atmospheric physics package of CESM2 and only the vertical resolution is being altered. The actual CAM7 release will have many additional changes including upgrades to a variety of physics parameterizations as well as a new dynamical core. These results should, therefore, not be taken as an indication of how CAM7 will behave; rather they represent an analysis of how the vertical resolution affects the representation of the atmosphere of CAM6. That being said, the model with additional physics changes is being tested to ensure that the dynamical behavior described here carries over to the next generation.

In section 2 we introduce the model, experiments and other model and observation-based datasets that we use for comparison. The diagnostics used are then introduced in section 3. In section 4 we present the results of the analysis of the impacts of vertical resolution on features of the tropical stratosphere which then motivates the final choice of vertical grids for CAM7, as summarized in section 5. In section 6 we introduce a new suite of experiments with this new grid above boundary layer (and CAM6's grid below) and check these simulations for the fidelity of stratospheric polar vortex variability and for any evidence of the QBO-MJO connection. Conclusions are then provided in section 7.

2 Methods

2.1 The model (CESM)

All model experiments documented here use CESM2 and a detailed description of this model can be found in Danabasoglu et al. (2020). The low-top atmospheric configuration within CESM2 is CAM6 and this simulates the atmosphere at approximately 1° horizontal resolution with 32 layers in the vertical stretching to a model lid at ∼40 km using the finite volume dynamical core (Lin & Rood, 1997). The high-top atmospheric component within CESM2 is WACCM6 which has a model lid at ∼140 km and 70 levels in the vertical. The vertical grids of WACCM6 and CAM6 can be seen in Fig. 1a. WACCM is typically run with interactive chemistry but a "specified chemistry" option, SC-WACCM, also exists which essentially reproduces the same climate as WACCM (Smith et al., 2014). Aside from the vertical grid, SC-WACCM differs from CAM in that greenhouse gases are specified as a lower boundary condition as opposed to a global concentration and are, therefore, advected by the atmospheric circulation. It also has a representation of methane oxidation, has specified shortwave heating rates taken from WACCM simulations above 65 km and, while both CAM and SC-WACCM have a parameterized representation of orographic gravity wave drag, SC-WACCM also has a representation of non-orographic gravity wave drag from convection and frontal sources (Richter et al., 2010). Since SC-WACCM contains features that are of relevance for the middle-atmosphere, we use the physics of the SC-WACCM component set instead of CAM6 in the majority of simulations presented here.

CAM and WACCM use a hybrid-sigma vertical coordinate that smoothly transitions from terrain following at the surface to constant pressure levels at around 170 hPa in CAM6 and 200 hPa in WACCM6. The grid is described by the hybrid coefficients (A and B) and for each vertical level (η) the pressure (in hPa) is given by

$$p(\eta) = A(\eta) \times 1000 \text{ hPa} + B(\eta) \times p_s \tag{1}$$

where p_s is the surface pressure (in hPa). A is zero at the surface and B becomes zero where the levels become constant pressure surfaces. For the finite volume dynamical core used in all the simulations presented here p is the actual (full moist) pressure, but for the spectral element dynamical core which will be used in CAM7, p will be the dry pressure and p_s will be the dry surface pressure (Lauritzen et al., 2018). The series of simulations that are used for the systematic investigation into the impact of vertical resolution on various features of the tropical atmosphere are summarized in Table 1 and the following section.

2.2 Vertical grid evaluations

Each of the grids that are used to evaluate the impacts of vertical resolution (Table 1) retain the same resolution as the default CAM6 within the boundary layer (the lowest 7 levels which extend up to about 850 hPa). Retaining the same levels in the boundary layer avoids re-tuning aspects of the model such as the shallow convection and microphysics schemes. Above the boundary layer, each of the grids that are evaluated consists of a constant resolution within the free troposphere and lower stratosphere that then tapers off to some specified value at the model lid following a hyperbolic tangent function.

The vertical grid spacing dz as a function of height is shown for the default configurations (CAM6 and WACCM6) in Fig. 1a. To produce Fig. 1, the height of each level (z) is calculated using $z = -H \, ln(p/p_o)$, assuming a scale height (H) of 7 km and a representative surface pressure (p_o) of 1000 hPa, with p computed using (1) assuming p_s=1000 hPa. The vertical grid spacing, dz, is then calculated by differencing the heights of adjacent levels. Both of these default configurations have $dz \sim$1137 m in the free troposphere. Above 100 hPa, dz for CAM6 tapers off very rapidly to about 6 km at the model lid ($\sim$40 km). WACCM6 has a higher resolution than CAM6 throughout the stratosphere and it decreases to $dz \sim$ 3.5 km at about 0.1 hPa and that resolution is then maintained up to the model lid ($\sim$140 km).

One of the primary goals of enhancing the vertical resolution within CAM is to improve the representation of the QBO, which has the potential to be an important source of predictability on the seasonal timescale. The study of Garcia and Richter (2019) demonstrated that enhancing the resolution to a grid spacing of $dz \sim$ 500 m achieved this goal. Retaining the high fidelity of the QBO representation is desirable, but so is computational efficiency, so here we investigate how the QBO behaves over a range of resolutions to find the optimum choice. To this end, the first phase of our analysis involves a suite of experiments where the grid spacing dz in the free troposphere and lower stratosphere is varied, from $\sim$1000 m to $\sim$400 m in increments of 100 m with the model lid at $\sim$140 km (Fig. 1b and Table 1). Note that the $dz \sim$500-m case is the same grid as the 110-level WACCM configuration of Garcia and Richter (2019). The resolution in each of these grids tapers off to a grid spacing of 3 km following a hyperbolic tangent function above $\sim$20 km. These simulations are run with prescribed observation-based sea surface temperatures (SSTs) (Hurrell et al., 2008) and without interactive chemistry (the SC-WACCM

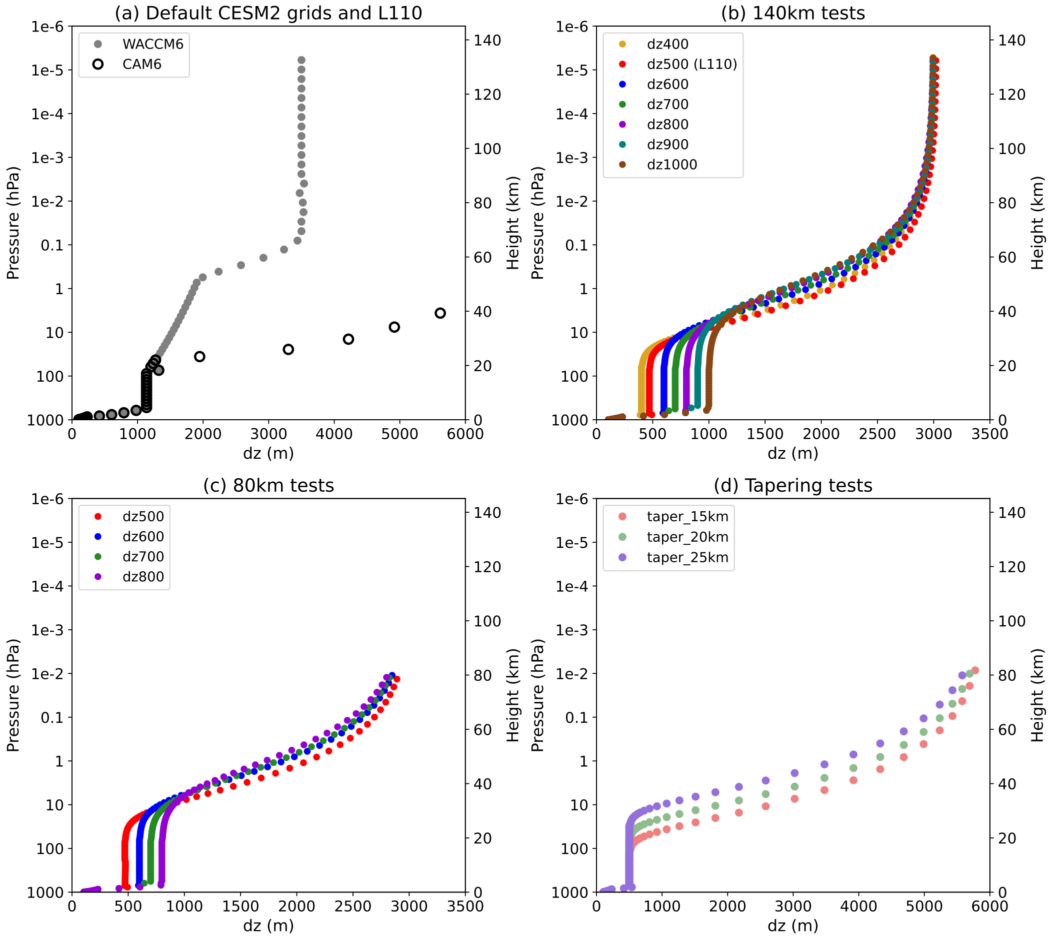

Figure 1. Grid spacing (dz in meters) as a function of pressure (left y-axis) or height (right y-axis) for (a) prior configurations used in CESM, and (b)-(d) the test cases used in this study. (a) shows the grid spacing for CESM2-WACCM6 and CESM2-CAM6. (b) shows the vertical resolution tests with the 140-km top, (c) shows the vertical resolution tests with the 80-km top, (d) shows the grids that are used to assess the effect of the level at which the vertical resolution is tapered.

Table 1. A summary of the simulations, periods of study, and number of members (when greater than 1) used in this study. From left to right the columns indicate the experiment name, the vertical grid spacing in the free troposphere, the approximate model lid height, the number of levels, and the simulation period with the number of members listed in parenthesis when greater than 1. Note that for the "80-km tapering experiment", the height at which the resolution starts to degrade is varied and for those simulations the vertical grid spacing degrades to 6 km at the model lid. For the 140 km tests, the resolution starts to degrade at 20 km but only degrades to a resolution of 3 km at the model lid. The * indicates that due to the loss of some data only 1988 to 2004 was used for calculations that involve the Transformed Eulerian Mean (TEM) diagnostics for dz1000 with the 140-km lid.

Name	dz (m)	approximate model lid (km)	# of levels	Simulation length
		CESM2 grids		
CAM6	1137	40	32	Coupled, 1979-2023 (50 mems)
WACCM6	1137	140	70	Coupled, 1979-2023 (3 mems)
				AMIP, 1979-2014 (3 mems)
		140-km grids		
dz1000	1000	140	84	AMIP, 1986-2004*
dz900	900	140	87	AMIP, 1986-2006
dz800	800	140	91	AMIP, 1986-2007
dz700	700	140	95	AMIP, 1986-2005
dz600	600	140	102	AMIP, 1986-2005
dz500	500	140	110	AMIP, 1986-2006
dz400	400	140	121	AMIP, 1986-2005
		80-km grids		
dz800	800	80	73	AMIP, 1986-2005
dz700	700	80	77	AMIP, 1986-2005
dz600	600	80	84	AMIP, 1986-2005
dz500	500	80	92	AMIP, 1986-2005
		80-km tapering experiments		
dz500_taper15km	500 to ∼15-km height	80	64	AMIP, 1979-1994
dz500_taper20km	500 to ∼20-km height	80	72	AMIP, 1979-1998
dz500_taper25km	500 to ∼25-km height	80	81	AMIP, 1979-1998
		L83 simulations (Grid shown in Fig. 14b)		
L83	500	80	83	AMIP, 1979-2020 (3 mems)
				Coupled, 1850-2100 (3 mems)

component set). They all start in 1986 and were run for between 19 and 22 years, depending on the simulation. All 140-km top configurations have the same gravity wave drag settings. There is, however, one exception to this. The upper boundary condition in the dz400 case was inadvertently set to deposit any remaining gravity wave momentum flux at the model lid, which was not done in the other 140-km top simulations but this setting has no noticeable impact on the features discussed and likely only has an affect close to the model lid because most of the gravity wave drag has already been deposited by 140 km. In practice, these gravity wave drag settings in a model with a new grid would be tuned to optimize the representation of the QBO and we have not done this here as tuning this number of separate configurations was impractical. We also focus our analysis on the role of the resolved waves which would be difficult to tune, as opposed to features like the QBO period, which can be relatively easily tuned through gravity wave drag settings. Given that these simulations are rather short, it is difficult to accurately assess the magnitude of the difference between any two configurations given the confounding impacts of internal variability. Instead, we take the approach of considering the distribution of simulations as a whole and assessing systematic variations as a function of vertical resolution across them.

The second step of our assessment of the impacts of vertical resolution then involves taking four of the resolutions dz ∼500, 600, 700, and 800 and lowering the model lid to ∼80 km, close to the top of the polar night jet. We take the same grids for these dz's as used for the 140-km top simulations, but discard the higher levels, retaining only those below 80 km (Fig. 1c and simulations described in Table 1, "80-km grids" section).These runs are each 20 years long, extending from 1986 to 2005. The gravity wave drag settings are the same as in the 140-km top simulations except that the upper boundary condition is changed, relative to the 140-km top simulations, such that the remaining gravity wave drag is now deposited at the model lid. This is a more appropriate choice for the 80-km model because much of the gravity wave drag in the polar vortex regions occurs around that level. If this momentum is not deposited at the model lid then momentum is not conserved within the model and the stratospheric mean meridional circulation will be too weak. These simulations are used to verify that the conclusions that are drawn as to the effect of dz on the QBO using the 140-km model lid hold when lowering the model lid height to 80 km and that the fidelity of the QBO is retained.

Finally, we assess the impacts of more drastically tapering off the resolution to 6 km at an 80-km model lid and the impacts of varying the height at which the degradation of the resolution begins following the hyperbolic tangent function. We run three further test cases with $dz \sim 500$ m and with the 80-km top, with the tapering to 6 km beginning at 25 km, 20 km and 15 km, respectively. These grids are shown in Fig. 1d and the simulations are summarized in Table 1, "80-km tapering experiments" section. Note that because the resolution is being tapered to dz ∼6 km, as opposed to 3 km in the previous tests, the degradation of resolution in the simulation is not comparable to that in the other 80-km test cases in terms of the impacts of tapering height. These runs begin in 1979 and run for between 16 and 20 years.

Unfortunately, an error was discovered in the gravity wave drag code that affects the aforementioned 140-km and 80-km top simulations. This is described in more detail in the supplementary text. In summary, due to this error, the simulations described above can only be used to examine features in the tropics such as the QBO and tropical waves, and cannot be used to examine the extra-tropical circulation or its variability. This error becomes relatively more important at higher vertical resolutions, so we have verified using the dz500 case with the 80-km top that it does not have an impact on the conclusions drawn regarding the wave driving of the QBO in supplementary Fig. S1. In the main text we show the 80-km top dz500 case with the error fixed.

2.3 L83 simulations

In section 6 we discuss a suite of simulations that have been performed with the chosen vertical grid for CAM7, but without the 10 additional levels that CAM7 introduces between the surface and 700 hPa. As will be described in more detail in section 6, this is an 83-level grid with 500-m grid spacing in the troposphere and lower stratosphere, tapering off to a 3.5-km resolution in the upper stratosphere and a model top at around 80 km as also shown in Fig. 14b. The resolution in the lower troposphere is unchanged from that of CAM6/WACCM6 to avoid re-tuning of the physics, allowing for a clean assessment of the impact of vertical resolution within CAM6. These simulations use CAM6 physics but with the non-orographic gravity wave drag scheme turned on (in addition to the orographic gravity wave drag scheme which is on by default in CAM6) and the upper boundary condition was changed such that any remaining gravity wave momentum flux at the model lid is deposited at the model lid (by default it passes through the lid in CAM6). Some minor adjustments were then made to the gravity wave drag settings to optimize the behavior of the QBO.

A coupled pre-industrial control simulation (not analyzed here) was branched from year 501 of the CESM2-CAM6 pre-industrial control. First, a short test run was performed for 8 years over which the simulation cools relative to CESM2, likely due to the reduced stratospheric water vapor with this grid (discussed in section 4.1.3). A 105-year long pre-industrial control was then continued from this short 8-year simulation and assessed for global mean temperature stability and a small and stable top of atmosphere (TOA) energy imbalance. The TOA imbalance was stable with an average imbalance of -0.043 Wm^{-2} (well within the tolerance limits typically used in CESM development) and the global mean temperature did not exhibit bigger trends over this 105-year simulation than the CESM2-CAM6 pre-industrial control does.

Three coupled historical simulations were branched from years 106, 100, and 103 of this pre-industrial control and run under CMIP6 historical forcings to the end of 2014, before being extended out to 2100 under the SSP3-7.0 projection scenario. Three simulations following the protocols of the Atmospheric Model Intercomparison Project (AMIP) with prescribed observation-based SSTs and sea ice (ERSSTv5 (Huang et al., 2017) for SST, HadISST1 (Rayner et al., 2003) and OISSTv2 (Reynolds et al., 2002) for sea ice) from 1979 to 2020, using CMIP6 historical forcings to 2014 and SSP3-7.0 forcings thereafter, have also been performed and are referred to as the “AMIP” simulations.

These simulations are used here to asses the impacts of the new grid on basic features of the stratospheric circulation and also to provide an assessment of the QBO-MJO connection in this configuration that now has a good representation of the QBO.

2.4 CESM2 simulations with CAM6 and WACCM6

The L83 simulations described above will be compared with simulations with CESM2-CAM6 and CESM2-WACCM6. For CESM2-WACCM6 we make use of the simulations that were performed for CMIP6 and these have fully interactive chemistry. This includes a 3-member ensemble of coupled historical simulations from 1850 to 2014 that are then extended to 2100 under the SSP3-7.0 scenario, as well as a 3-member ensemble of AMIP simulations from 1979 to 2014 with historical forcings and prescribed SSTs following Hurrell et al. (2008). For comparison with CESM2-CAM6 we use the coupled simulations from the CESM2 large ensemble (LENS2, Rodgers et al., 2021), specifically the first 50 members which have forcings comparable to the L83 simulations, i.e., from 1850 to 2014 using CMIP6 historical forcings and SSP3-7.0 forcings thereafter.

2.5 Observation-based data

One of the primary features of interest in this study is atmospheric waves in the tropical lower stratosphere and their role in driving the QBO. A complete observational record of waves in the tropical lower stratosphere is lacking given that they span a wide range of spatial and temporal scales. Satellite observations are capable of measuring waves with vertical wavelengths of the order of 4 km (Alexander & Ortland, 2010) but the tropical atmosphere also hosts wave motions with much finer vertical scales than this, as identified from balloon borne measurements (Vincent & Alexander, 2020; Bramberger et al., 2021). Atmospheric reanalyses are the only source of long-term, gridded, vertically resolved information but the observational constraints in the tropics are weaker than those in the extra-tropics given the reduced role for geostrophic balance, relatively fewer observations over the tropical oceans, and a lack of observations of sufficient vertical resolution to capture the details of tropical waves. As a result, the underlying model physics and dynamics are probably playing an important role in the resulting climate. While recognizing that atmospheric reanalyses are likely imperfect, we use them here as our source of observational comparison. We make use of three reanalysis products: ERA5 (Hersbach et al., 2020), MERRA2 (Gelaro et al., 2017), and JRA55 (Kobayashi et al., 2015). Our primary focus will be on ERA5 because it has a much higher vertical resolution than the other two products with grid spacings of the order 300 m in the troposphere compared to grid spacings of over 1000 m in the upper troposphere in MERRA2 and JRA55 (Supplemental Fig. S2). To the extent that the waves in the lower stratosphere may lack an observational constraint and instead would rely on model numerics successfully representing the propagation of wave activity produced by tropospheric diabatic heating into the stratosphere, we expect ERA5 to represent these more accurately given its higher resolution. Although, it is likely still deficient in representing the waves with very fine vertical scales (Bramberger et al., 2021). For some of the key analyses we provide a comparison with JRA55 and MERRA2 in the supplemental material. Prior to computing covariances from the reanalyses data, the wind and temperature fields were first regridded onto the $\sim 1°$ CAM6/WACCM6 grid to ensure a like-with-like comparison of fluxes associated with the same horizontal spatial scales.

We also make use of the Stratospheric Water and Ozone Satellite Homogenized (SWOOSH) database (Davis et al., 2016) for an observation-based estimate of stratospheric water vapor. This dataset extends from 1984 to 2023 but we only use the period of January 2005 to December 2021 as there are data gaps prior to the introduction of the Aura Microwave Limb Sounder data in 2005 and then the Hunga Tonga volcanic eruption in early 2022 resulted in a large perturbation in stratospheric water vapor (Niemeier et al., 2023). This means we are not comparing exactly the same time periods between SWOOSH and the simulations. While greenhouse gas-driven warming is expected to lead to an increase in stratospheric water vapor, the observational record does not exhibit a substantial trend between the period of the model simulations and the period we use for SWOOSH (Dessler et al., 2014), so a mismatch in time between the simulations and SWOOSH is unlikely to be important.

3 Diagnostics

3.1 Transformed Eulerian Mean diagnostics

To examine the wave driving of the QBO we use Transformed Eulerian Mean (TEM) diagnostics, following Gerber and Manzini (2016). The zonal wind tendency due to resolved waves is given by

$$\frac{\partial \overline{u}}{\partial t}_{\nabla \cdot \mathbf{F}} = \frac{1}{a\cos\phi}\nabla\cdot\mathbf{F} = \frac{1}{a\cos\phi}\left[\frac{\partial F_\phi cos\phi}{acos\phi\partial\phi} + \frac{\partial F_p}{\partial p}\right] \tag{2}$$

where

$$F_\phi = acos\phi \left\{ \frac{\partial \overline{u}}{\partial p}\psi - \overline{u'v'} \right\} \tag{3}$$

and

$$F_p = acos\phi \left\{ \left[f - \frac{\partial \overline{u} cos\phi}{acos\phi \partial \phi} \right] \psi - \overline{u'\omega'} \right\} \tag{4}$$

are the meridional and vertical components of the E-P flux in pressure coordinates. The vertical E-P flux that we show is actually the vertical E-P flux in log-pressure coordinates given by

$$F_z = -\frac{H}{p_o} F_p \tag{5}$$

where H is a scale height of 7 km and p_o is a reference surface pressure (1013.25 hPa). Overbars indicate zonal means, primes indicate deviations from the zonal mean and u, v, θ, and ω are the zonal wind, meridional wind, potential temperature, and vertical pressure velocity on constant pressure levels, respectively. Much of our analysis will focus on the role of the waves in driving the QBO, where the $\overline{u'\omega'}$ term dominates. The E-P fluxes (3) and (4) are computed using daily averaged eddy fluxes on a set of fixed pressure levels with the pressures of those levels equal to (1) with p_s set to 1000 hPa. The fluxes have been computed at each model timestep (every half hour) before averaging over the day. For ERA5, the fluxes are computed hourly and then averaged over the day.

3.2 QBO easterly to westerly transition composites

It will be shown below that the vertical resolution impacts the representation of the wave driving of the descending westerly phase of the QBO. To examine this, we produce composites of various fields prior to the time when the QBO transitions from easterly to westerly. When using monthly mean fields, the timing of this transition from easterly to westerly is determined simply as the month where the zonal-mean zonal wind averaged over 5°S to 5°N first transitions to westerly after having been below -0.5σ where σ is the standard deviation of that zonal wind field across months.

When using daily fields, the transition times are determined in the same manner as above but using 30-day running means instead of monthly values for the zonal wind and determining the transition as the center time of the first 30-day running mean that transitions above zero following a minimum in the 30-day running mean zonal-mean zonal wind that falls below -0.5σ where σ is the standard deviation across all 30-day running means. Similarly, the time at which the transition from westerly to easterly occurs is determined as the first 30-day running mean that transitions below zero following a maximum in the 30-day running mean that is greater than 0.5σ.

In section 4.1.2, to understand the behavior of Mixed Rossby-Gravity (MRG) waves, composites are calculated using 100-day running segments that are separated by 50 days (i.e., partially overlapping). The transition from easterly to westerly QBO for these composites is similarly defined as the center of the 100-day segment during which the average 5°S to 5°N zonal-mean zonal wind transitions to being positive for the first time after having been below -0.5σ where σ here is the standard deviation of the 100-day running averages, separated by 50 days.

3.3 Cospectra and power spectra

To quantify eddy fluxes as a function of zonal wavenumber and frequency, the cospectra method of Hayashi (1971) is used. When doing this analysis for composites prior to the time of transition to westerly QBO (t), the cospectra are calculated using the segment from $t-95$ to $t+5$ and a Hanning taper is used over the first and last five days of the segment. When the waves are examined climatologically, the timeseries are deseasonalized, using the first four harmonics of the seasonal cycle, and linearly detrended.

The cospectra are then computed over 100-day segments throughout the record that overlap by 60 days with tapering over the first and last 5 days, and then averaged. All cospectra, in both model and reanalysis, are computed using daily averages calculated as the average over 6-hourly instantaneous values as this is what was saved for the majority of the simulations.

4 Vertical resolution impacts

The simulations described in section 2.2 will now be assessed to determine the systematic impacts of tropospheric and lower stratospheric dz, the impacts of lowering the model lid, and the impacts of the level at which the degradation of the resolution begins on the representation of the QBO and other features of the tropical atmosphere.

4.1 Vertical resolution impacts with the 140-km top

4.1.1 The Quasi-Biennial Oscillation (QBO)

The QBO is a quasi-periodic reversal in sign of the zonal-mean zonal wind in the equatorial stratosphere. It is characterized by shear layers that descend from the upper stratosphere to the lower stratosphere with alternating westerly and easterly phases occurring over a period of about 28 months (Baldwin et al., 2001). It arises as a result of interactions between the zonal-mean flow and a variety of types of waves that are generated primarily through diabatic heating in the troposphere and transport of momentum up into the stratosphere. These waves are selectively filtered depending on the sign of the zonal-mean flow and deposit their momentum in regions of vertical shear, leading to the descent of zonal winds of one sign or the other (Holton & Lindzen, 1972). The descent of the westerly phase of the QBO is driven primarily by Kelvin waves and small-scale gravity waves, in roughly equal proportions while the small-scale gravity waves dominate in the descent of the easterly phase with lesser contributions from inertio-gravity waves and MRG waves (Giorgetta et al., 2002; Ern & Preusse, 2009; Alexander & Ortland, 2010; Kawatani et al., 2010; Ern et al., 2014; Y.-H. Kim & Chun, 2015; Pahlavan, Wallace, et al., 2021). In WACCM, Garcia and Richter (2019) found that the QBO actually acts to generate MRG waves.

It is increasingly common that models are now able to capture some form of internally generated QBO (Richter et al., 2020). However, the amplitude of the QBO in the lower stratosphere tends to be underestimated compared to observations (Richter et al., 2020; Bushell et al., 2020), and the most likely reason for this is a lack of vertical resolution (Holt et al., 2021) as evidenced by a number of studies that have demonstrated that enhanced vertical resolution leads to an improved representation of equatorial waves and their role in driving the QBO (Boville & Randel, 1992; Giorgetta et al., 2006; Richter et al., 2014; Anstey et al., 2016). Some of the waves that are responsible for driving the QBO have relatively short vertical wavelengths, of the order of 1 km (Bramberger et al., 2021), and as waves approach their critical level where they deposit their momentum, the vertical wavelength decreases further. Therefore, if a model has insufficient vertical resolution, numerical dissipation could lead to these waves being numerically damped below their critical level where their ability to accelerate the mean flow is diminished due to the greater atmospheric density (Vincent & Alexander, 2020). These past studies and theoretical understanding motivate the following assessment of the impact of vertical resolution on the representation of the QBO and the associated wave driving in CAM.

Figure 2 shows composites of monthly mean quantities in the equatorial stratosphere averaged from 5°S to 5°N in the 140-km top simulations, lagged relative to the month at which the QBO transitions from easterly to westerly at 50 hPa (see section 3.2). Firstly, the composites of the zonal-mean zonal wind reveal that as dz is decreased (resolution is increased), the westerly phase of the QBO descends further into the lower stratosphere (compare with the black line at 80 hPa in Fig. 2 top row). More quantitatively, the QBO amplitude metric of Dunkerton and Delisi (1985) (Fig. 3) is the smallest in the dz1000 and dz900 cases throughout the stratosphere. The dz800 case has an amplitude somewhere in the middle and then the dz700 to dz400 cases are all somewhat similar to one another and have the largest amplitudes without showing much systematic dependence on resolution. Therefore, as far as the amplitude of the QBO is concerned, the grid spacings greater than dz700 appear to be insufficient.

The ERA5 QBO exhibits a clear asymmetry in the duration of the easterly and westerly QBO phases. In the upper stratosphere, above about 30 hPa, the easterly phase is of longer duration than the westerly phase. The opposite is true in the lower stratosphere, where the westerly phase lasts longer (Fig. 2, top left). These two features are likely connected. Westerlies in the lower stratosphere suppress the upward propagation of parameterized gravity waves with eastward phase speed, so it is not until the lower stratospheric westerly phase weakens, that a westerly tendency due to gravity waves begins in the upper stratosphere to terminate the upper stratospheric easterly phase (Fig. 2 third row, compared with first row). A more prolonged westerly phase in the lower stratosphere, therefore, is associated with a more prolonged easterly phase above. This asymmetry in phase durations that is found in ERA5 is absent in the low resolution simulations, but becomes more apparent with increasing resolution. We note that there is some scope for tuning the average period of the QBO through gravity wave drag settings. However, it is unlikely to impact this asymmetry in the duration of phases, which apparently arises as a result of an enhanced role for resolved waves in driving the QBO and in persisting the duration of the westerly phase in the lower stratosphere, as now discussed.

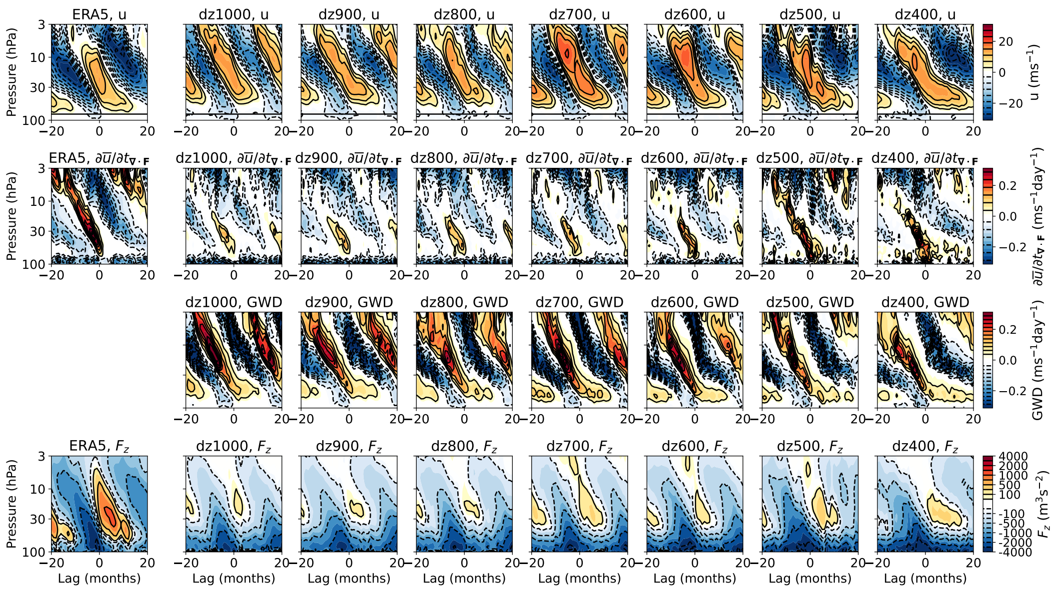

Figure 2. Composites of monthly averaged fields, area averaged from 5°S to 5°N and lagged relative to the month at which the zonal-mean zonal wind area averaged from 5°S to 5°N at 50 hPa transitions from easterly to westerly. The left column shows ERA5 and the remaining columns show the simulations with the 140-km top and dz ranging from 1000 m on the left to 400 m on the right. (top) zonal-mean zonal wind and the black horizontal line shows the 80 hPa level to guide the eye. (2nd) zonal-mean zonal wind tendency due to resolved waves, i.e., $\partial\overline{u}/\partial t_{\nabla\cdot\mathbf{F}}$. (3rd) zonal-mean zonal wind tendency due to gravity waves. (bottom) the upward component of the E-P flux, F_z.

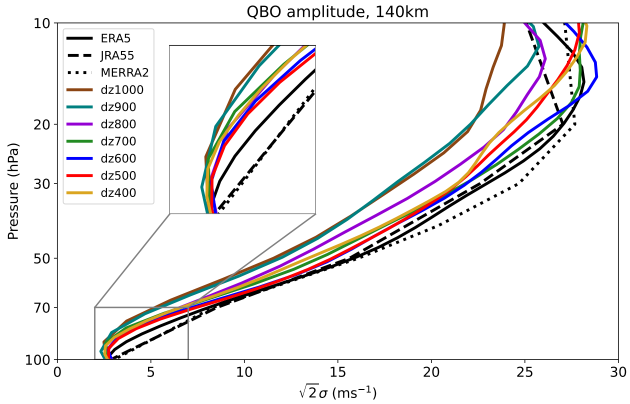

Figure 3. The Dunkerton and Delisi (1985) QBO amplitude ($\sqrt{2}\sigma$ where σ is the standard deviation of the deseasonalized zonal-mean zonal wind averaged from 5°S to 5°N) for ERA5 (black), JRA55 (dashed), MERRA2 (dotted) and the 140-km top simulations using area averaged 5°S to 5°N zonal-mean zonal wind. The inset zooms in on the region outlined by the gray box.

Both resolved waves (Fig. 2, 2nd row) and parameterized gravity waves (Fig. 2, 3rd row) contribute to driving the descent of the westerly and easterly phases of the QBO. Where we see the biggest impact of vertical grid spacing within CAM is on the role of the resolved waves in driving the descending westerly phase. In ERA5, the E-P flux divergence is positive throughout the depth of the stratosphere during the months prior to the transition of the equatorial winds from easterly to westerly. This is not well represented with a coarse vertical resolution, e.g., compare ERA5 and dz1000 in row 2 of Fig. 2. However, this is a feature that improves considerably as the resolution increases. The role of the resolved waves in driving the descending westerly phase becomes increasingly important in the lower stratosphere as we move toward higher resolution and the resolved waves start to play a greater role in the upper stratosphere as well. The model is still deficient in the magnitude of the contribution from resolved waves relative to ERA5 above 70 hPa, particularly in the upper stratosphere, but the dz500 and dz400 cases are improved compared to the lower resolutions.

The equatorial wave driving in the different resolutions can be compared more quantitatively in Fig. 4a which shows the tendency of the zonal-mean zonal wind due to the divergence of the E-P flux (Eq. 2) averaged over the 90 days prior to the transition from easterly to westerly at each level. This acceleration due to resolved waves increases more or less monotonically as a function of resolution. In the lower stratosphere, as we move from dz1000 to dz400 the acceleration of the westerlies due to resolved waves increases, although the higher resolutions tend to actually show a greater acceleration than ERA5. Higher up, the dependence on resolution is less systematic but, in general, the dz500 and dz400 cases show a greater acceleration of the westerlies due to resolved waves, although they both show a smaller magnitude compared to ERA5.

Latitude-pressure cross sections of the resolved wave driving for the 90 days prior to and after the transition from easterlies to westerlies at 50 hPa (Fig. 5) further demonstrate the dependence of the resolved wave driving on resolution throughout the tropics. Prior to the transition to westerlies at 50 hPa, the westerly acceleration due to resolved waves systematically increases with resolution. This brings the higher resolution grids closer to ERA5, yet all configurations show weaker tendencies than ERA5 indicating that either the model behavior has not yet converged with 400-m resolution or that there is another issue with the representation of wave forcing from below, for example,

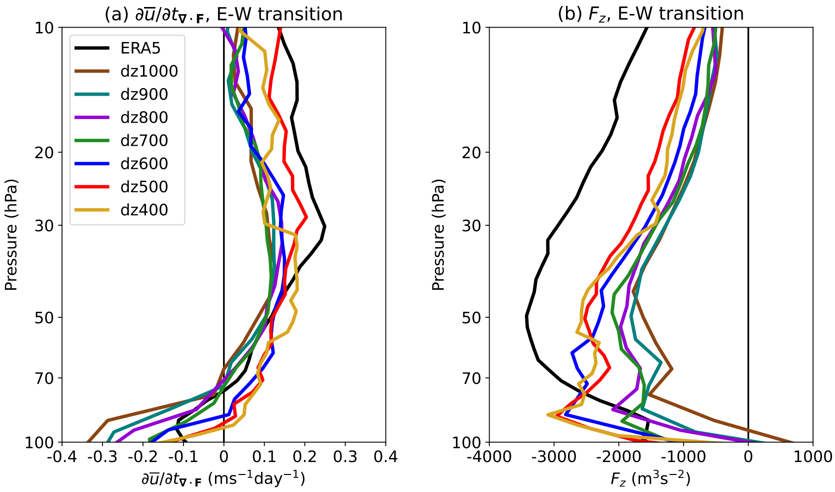

Figure 4. (a) Composites of the zonal-mean zonal wind tendency due to resolved waves (Eq. 2) for ERA5 and the 140-km top simulations for the 90 days prior to the transition from easterly to westerly determined separately at each level. (b) is as (a) but for vertical E-P flux component F_z.

insufficient forcing from higher-frequency Kelvin waves (Ricciardulli & Garcia, 2000). After the transition to westerlies at 50 hPa (Fig. 5, bottom row) the resolved waves in ERA5 continue to provide a westerly acceleration that acts to maintain the lower stratospheric westerlies. This westerly acceleration is absent in the lowest resolution model configurations, but emerges in the higher resolution cases. In fact, there is some indication that the dz500 and dz400 cases then have too much westerly acceleration from resolved waves after the transition to westerlies in the lower stratosphere (below about 70 hPa) compared to ERA5. The westerly acceleration that persists after the transition to westerlies in the lower stratosphere is likely playing a role in the more prolonged lower stratospheric westerly phase at high resolution compared to lower resolutions, leading to the asymmetry in the persistence of QBO phases of opposite sign in both the lower and upper stratosphere.

The resolved wave driving that occurs prior to the transition to westerlies stems primarily from convergence of the (negative) vertical E-P flux associated with upward propagating Kelvin waves. The bottom row of Fig. 2 shows that, as resolution increases, so too does the magnitude of the negative F_z in the months prior to the QBO transition. This can be seen more quantitatively in Fig. 4b where there is a clear dependency on vertical grid spacing of the magnitude of the negative upward F_z prior to the transition to westerlies. Again, the dz500 and dz400 cases are still deficient in the magnitude of the negative F_z compared to ERA5, but they are improved compared to the lower resolutions.

We further verify the impact of dz on the representation of equatorial Kelvin waves and their associated momentum fluxes by considering wavenumber-frequency cospectra or power spectra during the approximately 90 days prior to the transition from easterly to westerly at 50 hPa (see section 3.3). The vertical eddy momentum flux ($u'\omega'$) is the main contributor to the vertical component of the E-P flux (Eq. 4) in the tropics and panels (a)-(h) of Fig. 6 show the wavenumber-frequency cospectra of $u'\omega'$ for waves that are symmetric about the equator. Waves that are anti-symmetric about the equator do not play much role in this transition from easterly to westerly QBO (supplemental Fig.

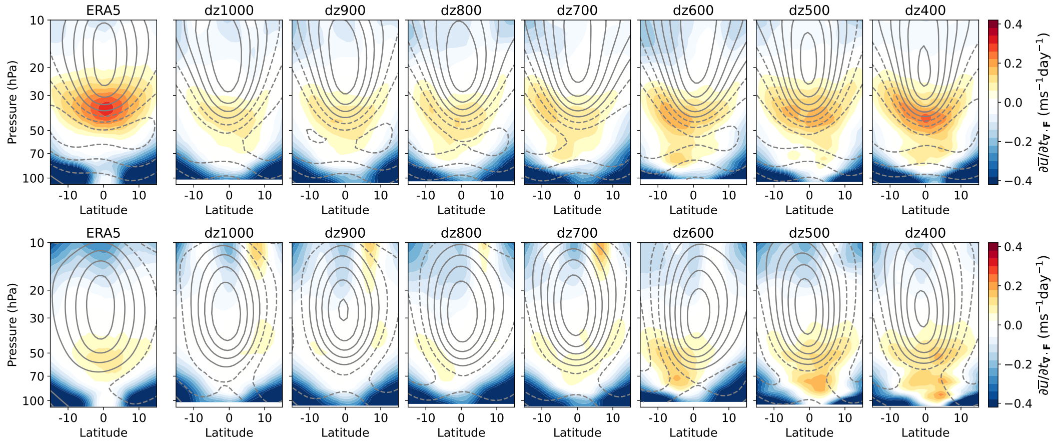

Figure 5. Latitude-pressure cross sections of the zonal-mean zonal wind tendency due to resolved waves (Eq. 2 in color shading) and the zonal-mean zonal wind (in contours with a contour interval of 4 ms^{-1} and dashed contours being negative and solid contours being zero or positive). The top panels show the composites for the 90 days prior to the transition to westerlies at 50 hPa and the bottom panels show the composites for the 90 days after the transition to westerlies at 50 hPa.

S3 shows the same but for the anti-symmetric waves). Figure 6 makes it clear that as resolution is increased in CAM, the negative $u'\omega'$, which dominates F_z increases to become closer to the magnitude of the momentum flux found in ERA5 in the Kelvin wave portion of this wavenumber-frequency space (see the diagonal gray lines at positive wavenumbers). A similar dependency on vertical resolution can be seen in the power spectra of the eddy vertical velocity in Fig. 6(i)-(p) indicating that the amplitude of the Equatorial Kelvin waves in the lower stratosphere is increased with higher resolution and becomes more aligned with that in ERA5. It makes sense that we should see enhanced power and associated momentum flux in the Kelvin wave portion of the spectra with increasing vertical resolution, given that these waves are typically characterized by relatively fine vertical scales and are, therefore, likely subject to more numerical dissipation at lower vertical resolutions (Holt et al., 2016; Vincent & Alexander, 2020). Indeed, this dependence on resolution is likely also apparent in the differences between the reanalysis datasets as the lower resolution JRA55 and MERRA2 have reduced Kelvin wave activity compared to ERA5 (supplemental Fig. S4).

Overall, these results suggest that there are improvements in the representation of the QBO with increased resolution both in the amplitude and the asymmetry in the duration of easterly versus westerly phases. This is likely related to an improvement in the role of resolved waves in driving both the descent of the westerly phase and the persistence of the westerly phase in the lower stratosphere. The results for the dz ~500 and dz ~400 cases are similar suggesting that any improvements to be seen by going to dz ~400 may not be worth the increased computational cost. On the other hand, the improvements in the representation of resolved wave driving of the QBO throughout the depth of the stratosphere with dz ~500 compared to lower resolutions suggest that it may be the preferable choice for balancing improvements in the representation of the QBO with computational expense.

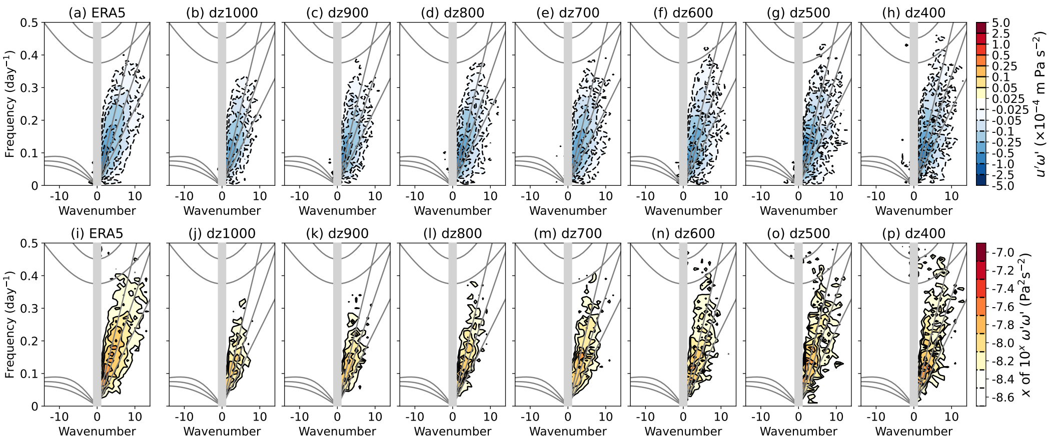

Figure 6. (a)-(h) Cospectra of the zonal-mean vertical eddy momentum flux at 50 hPa ($\overline{u'\omega'}$) averaged over 5°S to 5°N for motions that are symmetric about the equator expressed as a flux per 0.01 day^{-1} frequency by 1 wavenumber bin, calculated over the approximately 90 days prior to the transition from easterly to westerly at 50 hPa (see section 3.3 for the method). Left shows ERA5 and the panels show, from left to right, dz1000 to dz400. Note the non-linear contour interval. (i)-(p) are as (a)-(h) but showing the power spectra of ω on a logarithmic scale. The gray curves depict the dispersion curves for Kelvin waves, inertio-gravity waves, and equatorial Rossby waves for equivalent depths of 12, 25, and 50 m following Wheeler and Kiladis (1998), although the inertio-gravity wave curve for equivalent depth of 50 m lies outside of the plotting range. Gray shading is present at wavenumbers that are unresolved by the cospectra analysis.

4.1.2 Climatologies of tropical wave activity

In the above, we have demonstrated the impacts of vertical resolution on the waves that drive the QBO. Here we present the impacts of vertical resolution on tropical waves, climatologically over the number of years quoted in Table 1.

The power spectra for the component of the eddy vertical pressure velocity which is symmetric about the Equator (Fig. 7) highlights Kelvin waves, inertio-gravity waves, equatorial Rossby waves and, in the troposphere, the MJO. In the stratosphere (top row of Fig. 7) with increasing vertical resolution, there is greater power in the Kelvin wave part of the spectrum, aligned with what was seen for the easterly to westerly transition composites for the QBO. What is more apparent in these climatological power spectra is also the increase in power of the inertio-gravity waves with increasing resolution, as represented by the increase in power at frequencies greater than around 0.3 day^{-1} over a wide range of wavenumbers. In general, for the stratospheric symmetric power spectra, increasing resolution pushes the model more toward ERA5. Notably, the lower vertical resolution reanalyses (JRA55 and MERRA2) have reduced Kelvin wave and inertio-gravity wave activity compared to ERA5 (supplemental Fig. S5). In the troposphere the background power dominates so the bottom row of Fig. 7 shows the 500 hPa $\omega'\omega'$ spectral normalized by the background. It can be seen that there is little dependence of tropospheric Kelvin wave power on resolution and there is a deficit of power at high frequencies, regardless of vertical resolution, consistent with there being a missing source of waves from below (Ricciardulli & Garcia, 2000). There are hints at greater power in the MJO part of the spectrum (small positive wavenumbers and low frequencies) at higher resolution and this will be returned to below.

The power spectra for the component of the eddy zonal wind that is antisymmetric about the Equator (Fig. 8) highlights MRG waves. In the stratosphere (top row of Fig. 8) it is clear that enhanced vertical resolution leads to greater power in these waves. In contrast to the symmetric spectra, this enhanced power at higher vertical resolution pushes the model further away from ERA5, and these waves are also in better agreement among the reanalyses products (supplemental Fig. S5). As in the symmetric spectra, in the troposphere the background dominates and this background shows increasing power with resolution, on the high frequency end of the spectrum (not shown). Normalizing by this background, however, reveals that there is little systematic dependency of the power of the tropospheric MRG waves and inertio-gravity waves on resolution (bottom row of Fig. 8).

Why then do the stratospheric MRG waves show such a strong dependency on vertical resolution? Garcia and Richter (2019) argued using the 110-level WACCM that the QBO winds are barotropically unstable resulting in the generation of MRG waves in-situ in the stratosphere. According to this argument these waves are actually generated in the stratosphere, as opposed to propagating upward from below. In Fig. 9 we investigate whether the changes in the QBO that arise with increasing vertical resolution lead to a greater prevalence of barotropic instability, thereby enhancing MRG activity. The figure shows composites lagged relative to the time when the QBO transitions from easterly to westerly using 100-day running segments separated by 50 days. The zonal-mean MRG activity is calculated in each 100-day segment by first filtering the zonal wind to retain only the zonal wavenumbers from -6 to $+3$ and the frequencies between 0.2 and 0.4 day^{-1} (see Blue box in the top left panel of Fig. 8) and then calculating the standard deviation of this filtered zonal wind across the 100 days before taking the zonal average. The standard deviation of MRG filtered zonal wind increases with increasing vertical resolution, particularly at the edges of the QBO westerly jet (compare Fig. 9 middle and left columns). Aligned with the hypothesis of Garcia and Richter (2019) the greatest MRG activity occurs during the times when the zonal-mean barotropic vorticity gradient at the edges of the QBO westerly jet has the greatest probability of being negative (Fig. 9, right column). Furthermore, in the model, with increasing vertical resolution, the structure of the QBO winds is such that there is an increasing probability of a negative barotropic vorticity gradient, which is likely generating more MRG waves in-situ in the stratosphere. This contrasts with ERA5 where there is a much reduced probability of negative barotropic vorticity gradients (Fig. 9c) and weaker MRG activity (Fig. 9b) compared to the higher resolution simulations. This weaker wave generation is likely because the QBO winds are broader in latitude and, therefore, the curvature of the zonal wind is reduced. Pahlavan, Wallace, et al. (2021) previously also demonstrated a lesser role for MRG waves in the QBO of ERA5 compared to in WACCM. They hypothesize that the reason barotropic instability, and associated MRG waves, may be less prevalent in ERA5 compared to WACCM is because of differences in the gravity wave drag parameterizations and the assimilation in ERA5 which introduces a constraint on the large scale flow. They argue that in WACCM the gravity waves tend to drive unstable flow, in contrast to ERA5's gravity wave drag which tends to act to reduce instability by weakening and broadening the QBO westerly jet (Pahlavan, Fu, et al., 2021).

Returning now to the dependence of the MJO on vertical resolution, hinted at in Fig. 7, we show the standard deviation of the MJO-filtered 500 hPa vertical (pressure) velocity (ω) during DJF in Fig. 10. Here, the daily averaged ω has been filtered to retain only zonal wavenumbers 1 to 5 and periods between 20 and 100 days. The standard deviation across days in each DJF season is then calculated and the average of that standard deviation across DJF seasons is obtained. This demonstrates a very clear dependence of the variance in ω on these time and spatial scales on resolution, particularly in the region East of Australia. The variance increases, but it also shifts slightly poleward, to become more aligned with what is seen in ERA5 with higher resolution, although to the west of Australia all resolutions are deficient in MJO variance. Enhanced variance

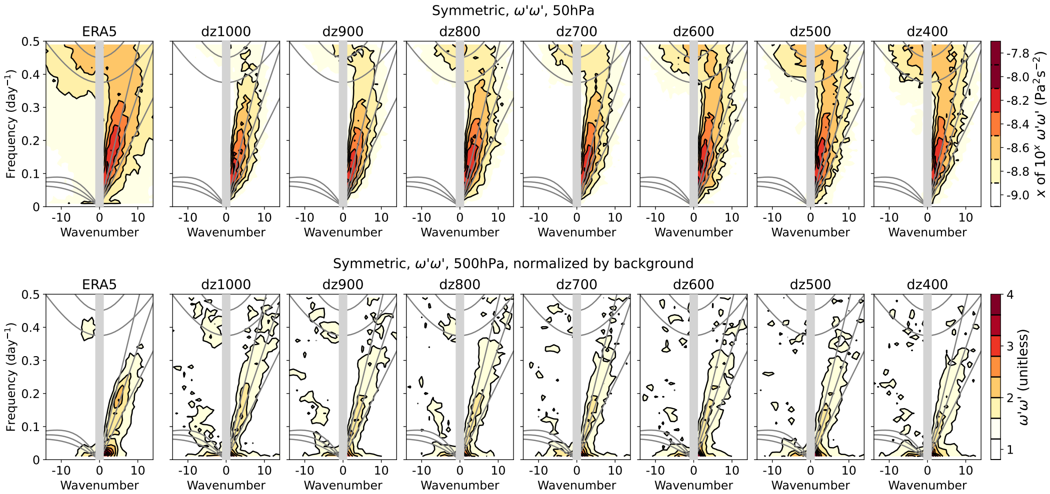

Figure 7. Power spectra of the component of the eddy vertical (pressure) velocity (ω') that is symmetric about the Equator, averaged from 5°S to 5°N. (Top row) at 50 hPa on a logarithmic scale, (bottom row) at 500 hPa after normalizing by the background (Wheeler & Kiladis, 1998). In the bottom row the power spectrum is smoothed with a two-dimensional Gaussian filter with a standard deviation of 1. The gray curves show the dispersion curves for Kelvin waves, inertio-gravity waves, and equatorial Rossby waves for equivalent depths of 12, 25, and 50 m and the gray shaded region depicts wavenumbers that are not resolved by the cospectra analysis.

in vertical velocity with increasing resolution might be expected due to the reduction in diffusive errors in the dynamical core's vertical remapping scheme (Lin, 2004) and/or improved representation of tropical waves of fine vertical scale and their role in the MJO with increasing resolution.

In summary, vertical resolution is found to lead to enhanced power in the Kelvin wave, inertio-gravity wave and MRG wave parts of the spectrum in the lower stratosphere. Taking ERA5 as the observational baseline, the enhanced power is an improvement for the Kelvin waves and the inertio-gravity waves, but is a degradation for the MRG waves, and this degradation likely arises due to increased barotropic instability of the QBO winds at higher resolution - a feature that is not so apparent in ERA5. Insofar as these MRG waves are a result of the QBO, as opposed to a driver of the QBO, this bias may not actually impact the simulation of the QBO itself(Garcia & Richter, 2019). There is also a clear dependency of the vertical motion associated with the MJO on resolution, with enhanced power at higher resolution, particularly in the region to the east of Australia, which leads to an improvement in this metric of the MJO when compared with ERA5, although all resolutions remain deficient in this metric in the Indian Ocean.

4.1.3 Stratospheric water vapor

Stratospheric water vapor also exhibits a strong sensitivity to vertical resolution (Fig. 11). As the resolution increases, the minimum in zonal-mean temperature in the upper-troposphere lower-stratosphere (UTLS) region decreases during the dry phase of the water vapor tape recorder (not shown) and the water vapor entering the stratosphere also reduces (Fig. 11). This dependence of stratospheric water vapor on resolution does mean that the higher resolution configurations are actually more biased compared to observations. However, there are various ways in which the stratospheric water vapor can

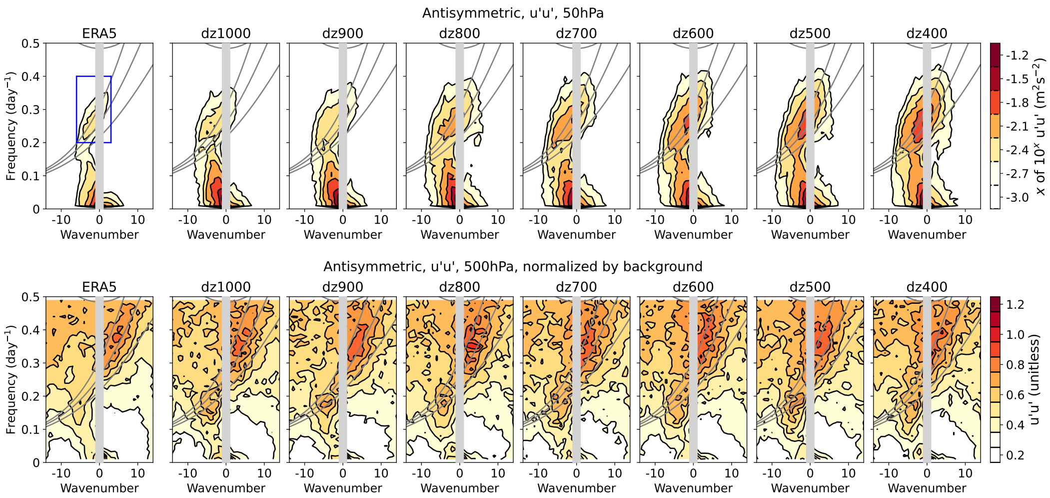

Figure 8. Power spectra of the component of the eddy zonal wind (u') that is antisymmetric about the Equator, averaged from 5°S to 5°N. (Top row) at 50 hPa on a logarithmic scale, (bottom row) at 500 hPa after normalizing by the background (Wheeler & Kiladis, 1998). In the bottom row the power spectrum is smoothed with a two-dimensional Guassian filter with a standard deviation of 1. The gray lines show the dispersion curves for mixed Rossby-gravity waves for equivalent depths of 12, 25, and 50 m and the gray shading masks out wavenumbers that are not resolved in the cospectra. The blue box in the top left panel shows the wavenumber-frequency range used for filtering in Fig. 9.

be tuned and in subsequent development versions of CAM, it has been possible to produce reasonable stratospheric water vapor climatologies with high vertical resolution (not shown). For example, we've found that increasing the convective time-scale in the Zhang-McFarlane deep convection scheme moistens the lower stratosphere.

4.1.4 Summary of vertical resolution impacts in the 140-km top simulations

In summary, in the 140-km top simulations, vertical resolution has a substantial impact on the QBO, waves and water vapor in the Equatorial stratosphere. Most of these impacts are positive. As we move toward higher resolution, resolved waves have a greater role in driving the QBO, especially Kelvin waves. Associated with this, the QBO extends deeper into the lower stratosphere and the asymmetry in the duration of the phases of the QBO appears with the westerly phase persisting longer in the lower stratosphere and the easterly phase persisting longer above. The enhanced resolution leads to more realistic amplitudes of Kelvin waves in the lower stratosphere and associated more realistic driving of the QBO by these waves. There also appears to be increased intraseasonal variance in the troposphere at the spatial and temporal scales associated with the MJO which is an improvement compared to ERA5, but the spatial structure of this variance is still deficient. However, as will be shown below, this spatial structure is improved in coupled simulations compared to the AMIP simulations used here. The enhanced amplitude of the QBO in the lower stratosphere does seem to be associated with a greater prevalence of barotropically unstable states, as found by Garcia and Richter (2019), which is connected with an increase in MRG activity. Both the presence of barotropically unstable states and the MRG activity seems to be over-done at the higher resolutions compared to ERA5. Stratospheric water vapor also degrades with increased resolution but

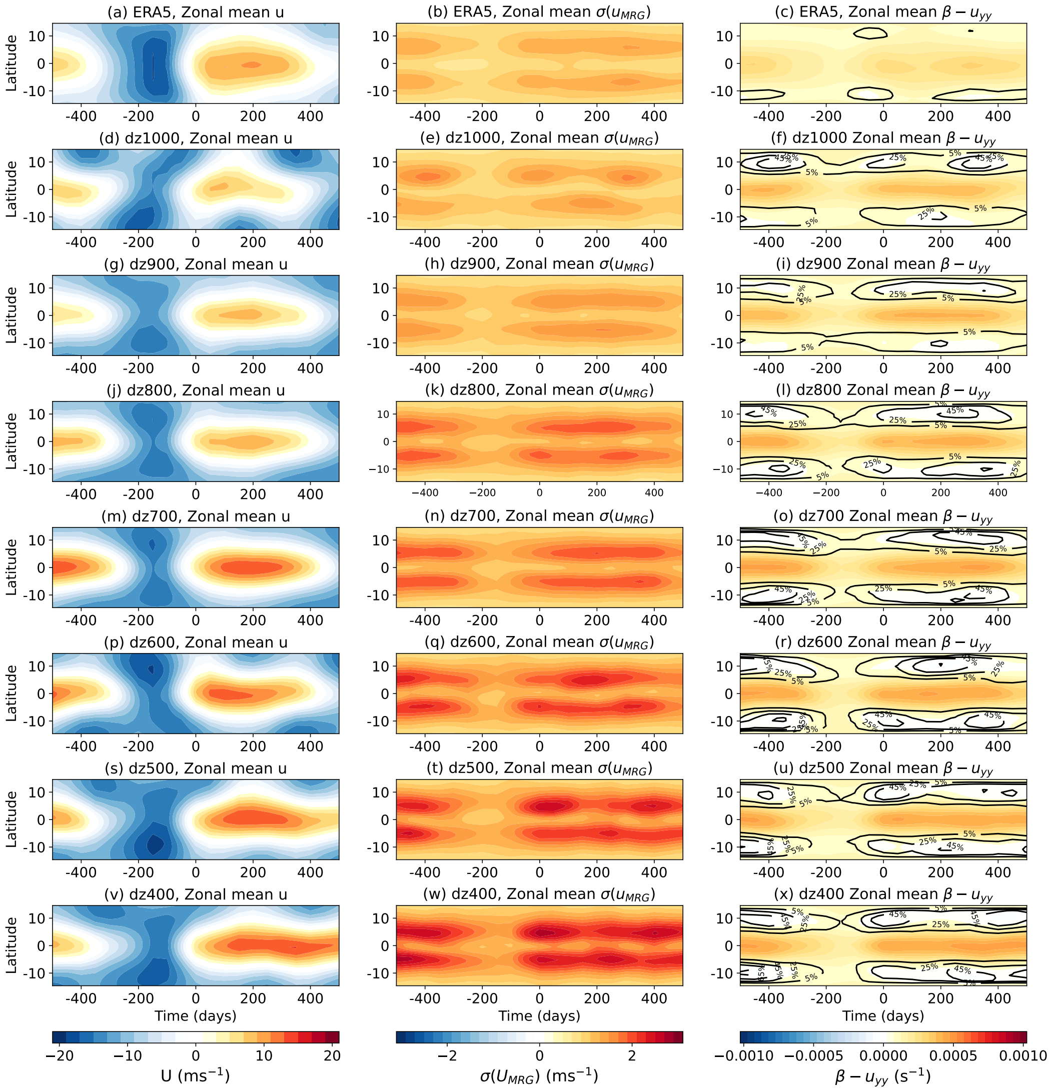

Figure 9. Composites of zonal-means of 100-day running averages separated by 50 days relative to the time at which the QBO transitions from easterly to westerly at 50 hPa (section 3.2). (left) Zonal-mean zonal wind at 50 hPa. (middle) The zonal-mean of the standard deviation of zonal wind at 50 hPa after filtering for MRG waves, i.e., retaining only zonal wavenumbers −6 to +3 and frequencies between 0.2 and 0.4 day^{-1} (see blue box in Fig. 8). (right) the zonal-mean barotropic vorticity gradient (shading) and the probability (percentage of days) of the zonal-mean barotropic vorticity gradient being negative. The zonal-mean barotropic vorticity gradient is given by $\beta - u_{yy}$ where the β parameter is the derivative of the Coriolis parameter with respect to latitude and u_{yy} is the second derivative of the zonal wind with respect to latitude.

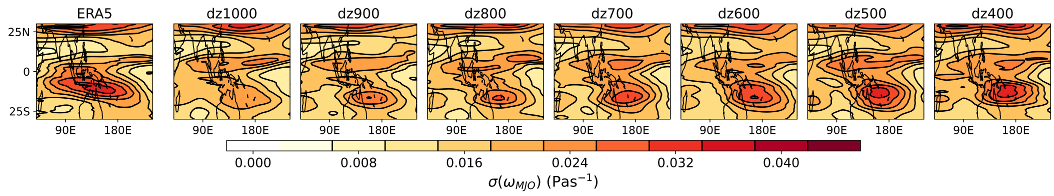

Figure 10. The standard deviation of MJO-filtered (zonal wavenumbers k=1-5 and periods=20-100 days) vertical (pressure) velocity at 500 hPa during DJF for (left) ERA5, (2nd-8th) dz1000 to dz400.

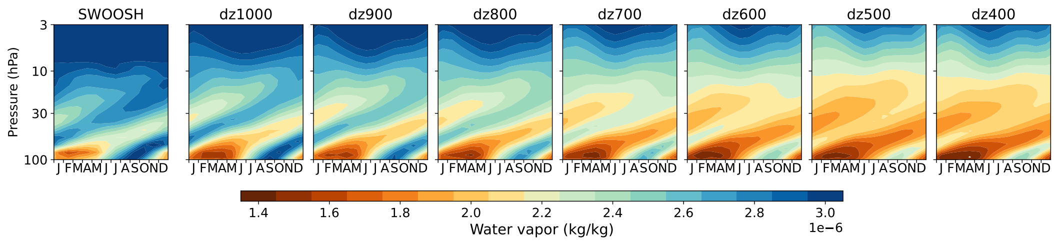

Figure 11. Zonal-mean specific humidity seasonal cycle area averaged from 5°S to 5°N. The left panel shows the observational SWOOSH dataset (Davis et al., 2016) using Jan 1st 2005 to December 31st 2021. The remaining panels show the 140-km top simulations from lowest to highest resolution.

there are other ways in which this can be tuned to lead to more realistic values. Overall, we consider the improvements in Kelvin waves and their role in driving the QBO and the overall QBO structure to be strong motivations for choosing a vertical resolution in the realms of the dz500 case.

4.2 What happens to the QBO if we lower the model top to 80 km and further degrade the resolution in the stratosphere?

There are two primary motivations for lowering the model top to about 80 km: (1) computational efficiency, particularly if we choose to reduce dz given the benefits this has to the QBO, and (2) ease of initialization of forecasts from reanalysis datasets. We therefore, now investigate whether the same conclusions can be drawn as to the representation of the QBO and the improvements associated with increasing resolution (decreasing dz) when lowering the model top to 80 km using dz=800, 700, 600, and 500 m.

The same QBO composite analysis as in Fig. 2 is shown for the 80-km top cases in Fig. 12 and the QBO amplitude for these cases shown in Fig. 13a can be compared with that of the 140-km top cases in Fig. 3. The equivalents of Figs. 4 to 6 for these 80-km cases are also shown in supplemental Figs. S6 to S8. The representation of the QBO is very similar between the 140-km model top and the 80-km model top and the same conclusions can be drawn as to the improvements associated with resolved waves driving the descending westerly phase of the QBO with increasing resolution. There are marked improvements in the representation of the resolved wave drag prior to the transition from easterlies to westerlies in going from dz ∼600 to dz ∼500 with both the 140-km model top and the 80-km top (Figs. 2 and 12, 2nd row). This suggests that, at least as far as the QBO is concerned, the model top can be lowered to 80 km without major detrimental effects. This will also be verified for polar vortex representation in section 6.

Figure 13b demonstrates that issues arise if the resolution is tapered to coarser grid spacings too low in the stratosphere. This shows the results of the sensitivity experiments with the degradation of vertical resolution to 6 km beginning at three different heights (Fig. 1d). It is clear that if the resolution is degraded at too low a level in the lower stratosphere, the QBO amplitude decreases considerably in the mid- and upper-stratosphere.

5 The chosen grid

Despite some other features that appear to degrade with increased resolution, such as the power in the MRG waves, we consider the improvements in the Kelvin waves and their role in driving the QBO to be sufficient motivations to choose a grid spacing of 500 m in the troposphere and lower stratosphere for CAM7. The more incremental improvements in tropical wave activity and its role in the QBO by going to an even finer resolution in the 400-m case was deemed to not be worth the additional computational expense. It is clear that reducing the resolution too much in the stratosphere can degrade the simulation of the QBO (Fig. 13b) and, in addition, to allow the possibility for WACCM to be built on top of CAM, it was concluded that it is preferable to not degrade the res-

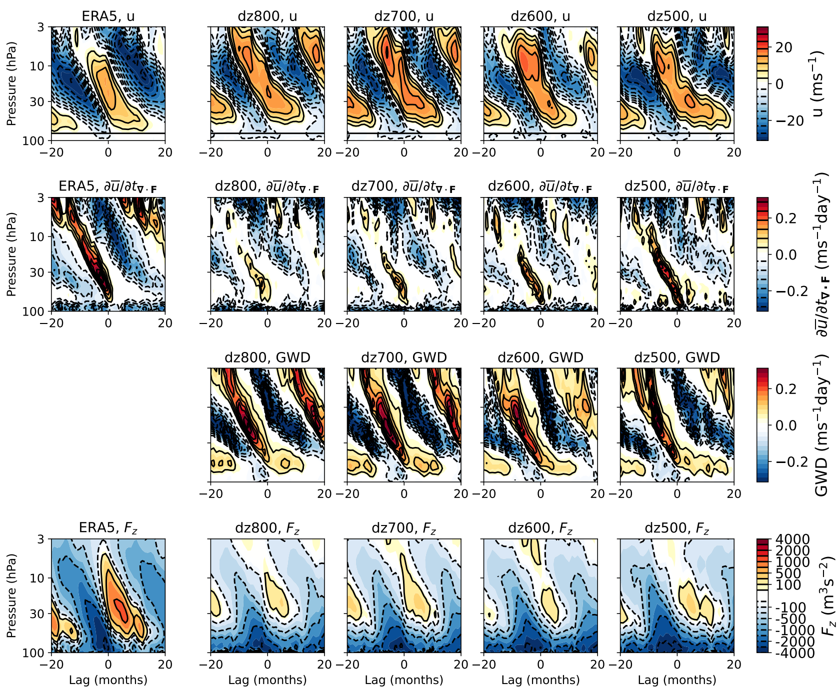

Figure 12. As Fig. 2 but for the simulations with the model top at ∼80 km. Composites of monthly averaged fields, area averaged from 5°S to 5°N and lagged relative to the month at which the zonal-mean zonal wind area averaged from 5°S to 5°N at 50 hPa transitions from easterly to westerly. The left column shows ERA5 and the remaining columns show the simulations with the 80-km model top and dz ranging from 800 m on the left to 500 m on the right. (top) zonal-mean zonal wind and the black horizontal line shows the 80 hPa level to guide the eye. (2nd) zonal-mean zonal wind tendency due to resolved waves, i.e., the E-P flux divergence (Eq. 2). (3rd) zonal-mean zonal wind tendency due to gravity waves in the model, and (bottom) the upward component of the E-P flux F_z.

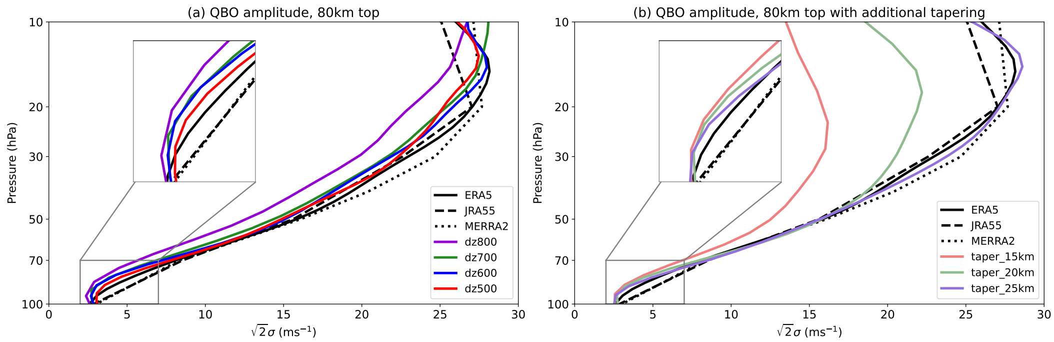

Figure 13. As Fig. 3 but for the simulations with the 80-km top. (a) The Dunkerton and Delisi (1985) QBO amplitude for ERA5 (black) and the 80-km top simulations with the model top lowered relative to the 140-km top simulations but no additional tapering, using area averaged 5°S to 5°N zonal-mean zonal wind. The inset zooms in on the region outlined by the gray box. (b) is as (a) but for the 80-km top simulations with dz500 and additional tapering of the resolution to 6 km at the model lid where the tapering begins at various heights, as summarized in the "80-km tapering experiments" section of Table 1 with the grids shown in Fig. 1d. Three reanalyses (ERA5, JRA55, and MERRA2) are shown in black.

olution beyond half a scale height (approximately 3.5 km) as this is the desired resolution for WACCM in the upper stratosphere and mesosphere.

Taken together, all these considerations have led to the final grid choice for the "mid-top" (MT) version of CAM7 shown in Fig. 14a (red). This has 500-m grid spacing in the troposphere, which then tapers off to a resolution of 3.5 km at about 45 km height. This 3.5 km grid spacing is then maintained up until the last three layers in which the resolution is degraded further since these lie within the sponge layer anyway.

In addition to these changes in the free tropospheric and stratospheric resolution motivated by the above analysis, the resolution is further increased in the lower troposphere (boundary layer). While the changes to the boundary layer resolution are not the focus of this study, we briefly summarize them here to provide a complete summary of CAM7's vertical grid. The changes to the boundary layer are shown in the inset of Fig. 14a and the lowest model level is lowered to be around 17 m (CAM6's lowest model level was around 52 m). As noted in the Introduction, there are multiple motivations for increasing resolution near the surface (see also McTaggart-Cowan et al. (2019)). Additionally, as can be seen in Fig. 14a, the CAM6 vertical grid spacing changed non-smoothly near 850 hPa. Considering the simple finite differencing done in the vertical in many of the atmospheric parameterizations, this non-smooth grid may introduce numerical error which may be alleviated by a more smoothly varying grid (e.g., Sudqvist & Veronis, 1970). Therefore, a stretched-grid algorithm was applied to distribute 10 additional levels below about 700 hPa such that the grid spacing increases and smoothly merges with the mid-tropospheric grid of the 83-level configuration to be discussed next (Fig. 14a inset). The end result of combining these enhancements in the boundary layer with the increased resolution in the free troposphere and stratosphere is a model that has 93 levels.

For tuning purposes and for users wishing to reduce the computational expense, a "low-top" (LT) 58-level configuration will also be made available (Fig. 14a, blue) in which the resolution tapers more drastically from the upper troposphere to a model lid at about 40 km, i.e., similar to CAM6's model top. The grid spacing below about 9 km

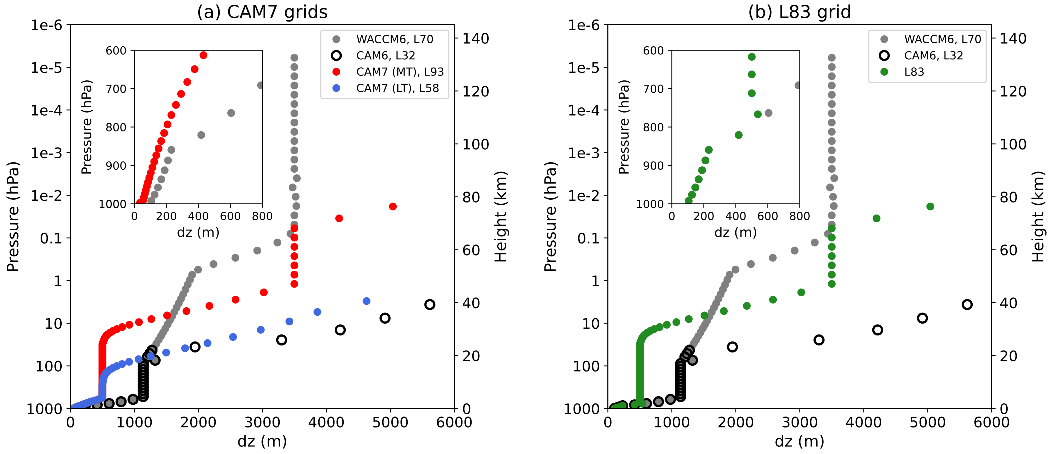

Figure 14. (a) Vertical grid spacing of the CAM7 configurations: the mid-top configuration (MT) in red, and the low-top configuration (LT) in blue. The existing CAM6 and WACCM6 grids are also shown for reference. The inset highlights the boundary layer grid spacing and only shows CAM7 (MT) and WACCM6 since they are the same as CAM7 (LT) and CAM6 in this region. (b) The L83 grid which has the same grid spacing as the new CAM7 grid above 850 hPa but the grid spacing of CAM6 below.

is the same in the MT and LT configurations so that the same tuning parameters for the physics schemes can apply to both.

6 L83 simulations

Changing the vertical resolution below about 850 hPa requires re-tuning of the model and some changes to the way in which the deep convection scheme behaves. Such changes will be present in CAM7 when it is released, along with a myriad of other changes such as the spectral-element dynamical core instead of the finite-volume dynamical core used in CAM6. As a result, CAM7 will be a rather different model from CAM6 and a clean assessment of the impacts of this new model grid will not be possible by simply comparing CAM7 with CAM6. We have, therefore, performed a suite of coupled historical and AMIP simulations using the new vertical grid, but without the additional levels in the boundary layer, described in section 2.3. This grid, referred to as L83, has 83 levels and is shown in Fig. 14b. The levels below 880 hPa match those of CAM6 but they transition to the 500 m grid spacing above that and match the proposed grid for CAM7 at the point where CAM7's grid spacing reaches 500 m. One of the coupled members and the AMIP simulations have already been analyzed by H.-K. Lee et al. (2024) to explore future projected changes in the QBO. This model has also been used to perform experiments for the QBO-intercomparison project (QBOi). Here, we use these simulations to demonstrate that the same improvements in the representation of the QBO are found as in the vertical resolution evaluation cases above, and also to show that the climatology and variability of the stratospheric polar vortices are improved compared to the low-top CAM6 and are more aligned with the behavior of WACCM6. In light of the fidelity of the QBO in this model, we also assess it for the existence of the QBO-MJO connection.

6.1 The QBO

Figure 15 shows composites of the zonal-mean zonal wind, the zonal mean zonal wind tendency due to resolved waves (Eq. 2), and the vertical component of the E-P flux lagged relative to the month when the QBO winds at 50 hPa transition from easterly to westerly, analogous to those shown in Figs. 2 and 12 but now for the L83 simulations. The QBO in the AMIP simulations (Fig. 15a-c) is rather similar to that in the vertical resolution sensitivity experiments presented above, with an important role for resolved waves in driving the transition from easterly to westerly, a QBO amplitude that is comparable to ERA5 (Fig. 15g), and a period that is also rather similar to ERA5 with a longer easterly phase than westerly phase in the upper stratosphere and vice-versa in the lower stratosphere. The coupled simulations similarly have an important role for resolved waves in driving the descending westerly phase and a good QBO amplitude. However, the QBO in the coupled simulations has a bit higher frequency than the AMIP simulations, likely due to differences in the representation of convectively generated gravity waves between them. Overall, the L83 grid, which is the CAM7 grid without changes to the boundary layer, has a good representation of the QBO in both coupled and AMIP mode and further refinements to the overall period may be possible with additional tuning of the gravity wave drag parameterizations.

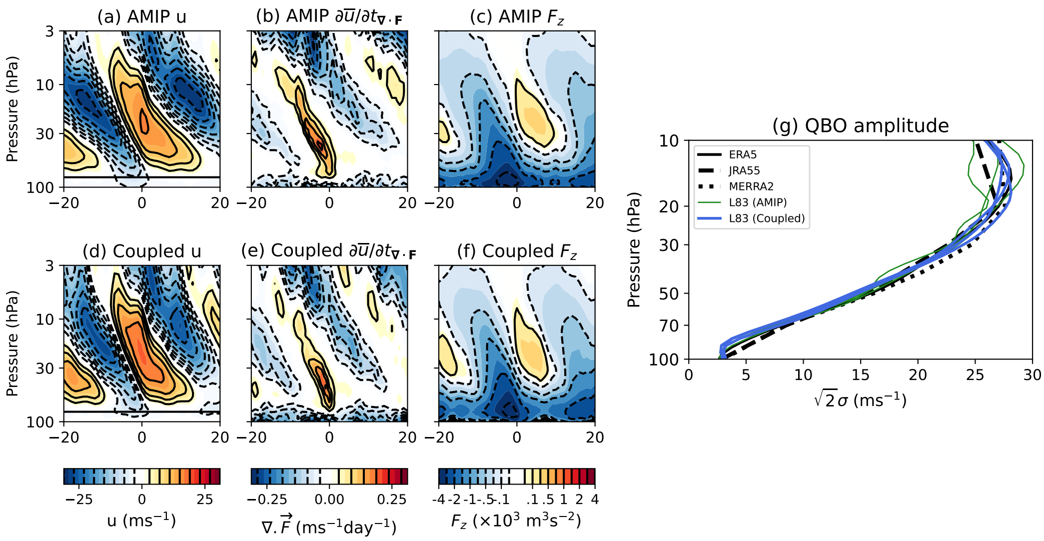

Figure 15. The representation of the QBO in the L83 simulations. (a)-(f) show composites of fields averaged from 5°S to 5°N lagged relative to the month at which the zonal-mean zonal wind averaged from 5°S to 5°N at 50 hPa transitions from easterly to westerly. (a) zonal-mean zonal wind, (b) E-P flux divergence (Eq. 2), and (c) vertical component of the E-P flux F_z for the AMIP simulations using 1979 to 2020. (d)-(f) are as (a)-(c) but for the coupled simulations using 1980 to 2023. (g) The Dunkerton and Delisi (1985) QBO amplitude for the reanalyses (black lines) and the three L83 AMIP members for 1979 to 2020 (green) and the three L83 coupled members for 1979 to 2023 (blue).

6.2 Other aspects of the stratospheric circulation

Figure 16 provides a comparison of the representation of the stratospheric polar vortices between the L83 simulations, the WACCM6 simulations, LENS2, and the reanalyses. This allows us to assess how this new grid with its 80-km model lid compares to the WACCM6 and LENS2 simulations with lids at ∼140 km and ∼40 km respectively. For the wintertime climatologies (Fig. 16a-f), the L83 simulations and WACCM6 are very similar. The biases that exist in L83 are similar to those in WACCM6, namely a Southern Hemisphere polar vortex that is too strong and westerlies that are too weak in the "neck" region between the tropospheric jet and the NH polar vortex.

For the polar vortex strength, L83 is, however, considerably improved compared to the low-top LENS2, as can be seen from the seasonal cycle of 10 hPa zonal-mean zonal wind averaged over 60° to 70° of latitude (Fig. 16g and h). Both the SH and NH polar vortices are too strong in LENS2. Both WACCM6 and L83 are much closer to the reanalyses, with a much smaller strong bias in the SH and a weak bias during the early winter in the NH leading to a maximum strength that peaks too late in the season, but L83 mostly lies within the WACCM6 range.

Figures 16i and j show the standard deviation of daily zonal-mean zonal wind. The variability in the SH vortex maximizes during the spring as the vortex breakdown occurs and this is relatively well represented in all simulations, including LENS2. In the NH, however, the low-top LENS2 simulations have too much variability during the late winter, which is improved in WACCM6 and L83. Both L83 and WACCM6 exhibit slightly reduced zonal wind variability in the mid-winter compared to reanalyses but they are very similar to each other and L83 lies within the WACCM6 range, albeit close to its upper limits. While the quantification of stratospheric sudden warming (SSW) frequency is subject to considerable uncertainty over the single observational record (as indicated by the range of values from LENS2 in Fig. 16k) there is general agreement in the SSW statistics between WACCM6 and the L83 configuration (Fig. 16k). Both underestimate the SSW frequency in January and February, in agreement with the reduced variance in polar vortex winds relative to observations (Fig. 16j) and both may be overestimating the SSW frequency in March, perhaps related to the polar vortex being stronger during this month than in observations leading to a higher chance of having an SSW that then recovers again prior to the final breakdown.

The Transfomrmed Eulerian Mean mass stream function is also rather similar between WACCM6 and L83 and both agree well with ERA5 reanalysis, in contrast to the low-top LENS2 in which the TEM streamfunction is stronger than observed in both NH and SH winter and is significantly distorted near the model top (Fig. 17).

Overall, these results suggest that the representation of other aspects of the stratospheric circulation is similar between L83 and WACCM6, indicating that a model top at 80 km does not lead to substantial degradations in features of the stratospheric circulation compared to the 140-km top of WACCM6, but at the same time it leads to improvements over the 40-km top of CAM6.

6.3 The QBO-MJO connection

In light of the improved fidelity of the QBO representation within the L83 configuration, we now assess the coupled and AMIP ensembles for their representation of the QBO-MJO connection. The QBO-MJO connection was first identified by Yoo and Son (2016). In reanalysis products they found that, during boreal winter, various MJO metrics indicate that the MJO is stronger than average during easterly QBO and weaker than average during westerly QBO. This connection is, however, not represented in free running ESMs (J. C. K. Lee & Klingaman, 2018; H. Kim et al., 2020; Z. K. Martin et al., 2023). It is weak (Abhik & Hendon, 2019; Z. Martin et al., 2020b) or insignificant (H. Kim et al., 2019) or absent (Andrews et al., 2023) in initialized hindcasts, and is still not well understood (Z. Martin et al., 2021).

Figure 18 shows the standard deviations of the daily MJO-filtered (zonal wavenumbers k=1-5 and periods 20-100 days), 500-hPa vertical velocity in isobaric coordinates

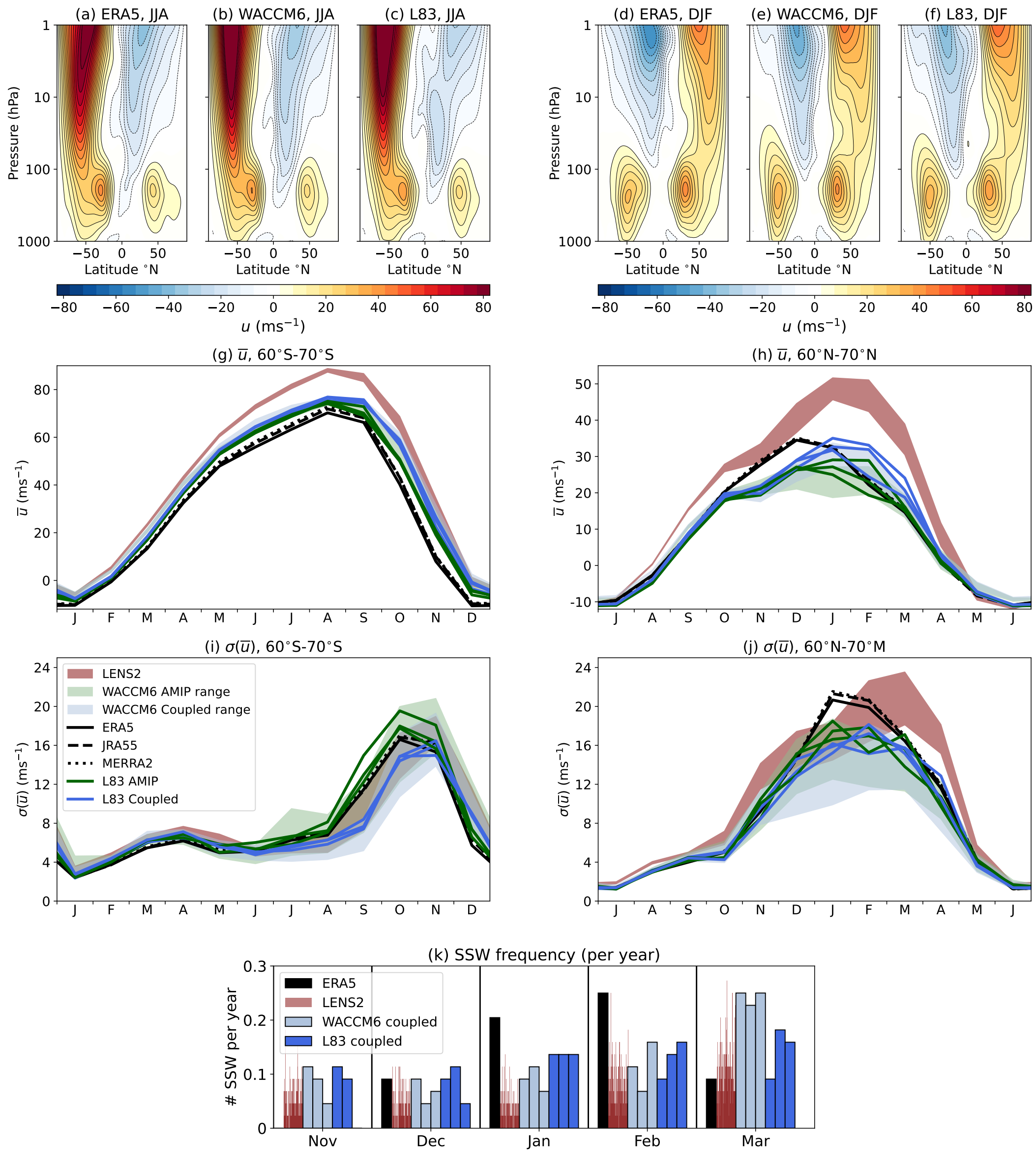

Figure 16. (a) Zonal-mean zonal wind during JJA for (a) ERA5, (b) the average of the 3-member WACCM AMIP ensemble, and (c) the average of the 3-member L83 AMIP ensemble. (d)-(f) are as (a)-(c) but for DJF. (g) Monthly climatologies of 10 hPa zonal-mean zonal wind averaged from 60°S to 70°S. The green and blue shaded ranges show 95% confidence intervals for WACCM6 AMIP and Coupled configurations determined by pooling together the years from the three members and bootstraping N years with replacement 1000 times to obtain 1000 climatologies for N year samples, where N is the number of years from 1979 to 2023 for the coupled simulations and from 1979 to 2014 for the AMIP simulations. The 5th to 95th percentile range across the LENS2 members is shown by the maroon shading. Reanalysis climatologies for 1979 to 2023 are shown in black and the climatologies for the L83 AMIP members from 1979 to 2014 are shown in green and for the L83 coupled members from 1979 to 2023 are shown in blue. (h) is as (g) but for the average from 60°N to 70°N. (i) and (j) are as (g) and (h) but showing the standard deviation of daily zonal-mean zonal wind for each month of the year determined by pooling together the daily values for a given month across all years and then calculating the standard deviations. (k) shows the SSW frequency (per year) over 1979 to 2023 for ERA5, the 100 members of LENS2 (thin salmon bars), the three WACCM coupled simulations (thick light blue bars), and the three L83 coupled simulations (thick dark blue bars).

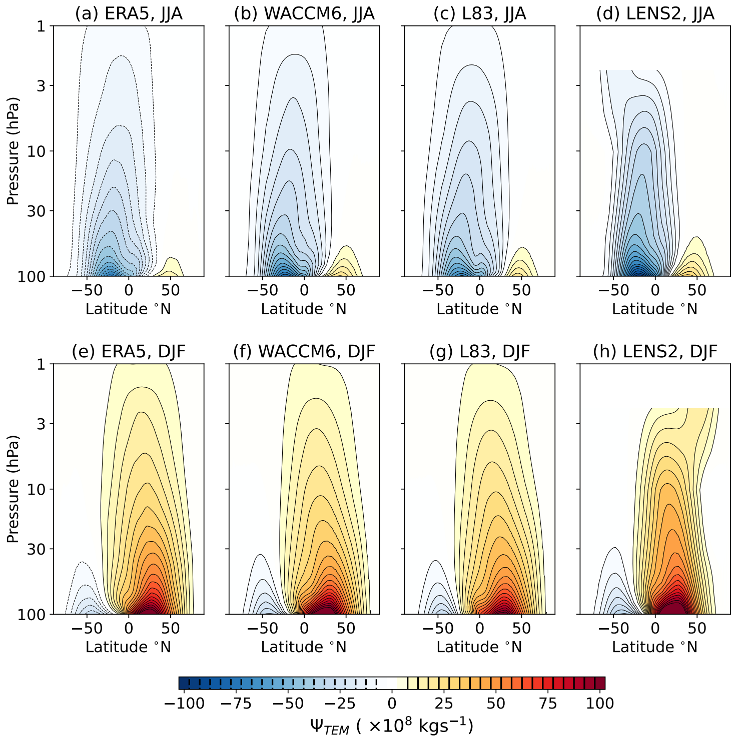

Figure 17. The transformed Eulerian Mean (TEM) stream function. (a)-(d) shows the JJA season for ERA5, WACCM6, L83, and LENS2 and (e)-(h) are the same but for the DJF season.

($\sigma(\omega_{500})$), computed for each DJF season and then averaged, as a metric of QBO variability (as also shown in Fig. 10). In ERA5 (Fig. 17a), this highlights the MJO activity that occurs around the maritime continent region to the north of Australia. We define QBO easterly and westerly winters as those where the anomalies from climatology in the 5°S to 5°N DJF-averaged, zonal-mean zonal wind at 50 hPa are less than -0.5σ and greater than 0.5σ, respectively, where σ is the standard deviation of the DJF averages of 5°S to 5°N zonal-mean zonal wind. Figure 18d demonstrates the observed connection between the QBO and the MJO by showing the difference in $\sigma(\omega_{500})$, i.e., a metric of MJO variability, between the QBO easterly and westerly years for ERA5. During QBO easterly years there is more MJO-filtered variance in vertical velocity compared to westerly years. This is a similar connection to that found by Yoo and Son (2016) except they used Outgoing Longwave Radiation (OLR). We show the same figure but for OLR in supplemental Fig. S9 and similar conclusions can be drawn using that variable although there is greater disagreement among the reanalyses.

The climatological MJO-filtered $\sigma(\omega_{500})$ in the coupled L83 simulations is represented reasonably well but with some overestimation in the Indian Ocean (Fig. 18b). In contrast, $\sigma(\omega_{500})$ is underestimated in the Indian Ocean in the AMIP simulations and is weaker over the Maritime Continent and to the northeast of Australia than in both ERA5 and the L83 coupled simulations (Fig. 18c). However, compared to the large scale circulation that we have examined here, the thermodynamics-based decomposition and pattern correlation of the MJO (convection, clouds, radiation) tends to perform more poorly (Li, 2022) and further examination of this is beyond the current scope. Considering now the difference between the QBO easterly and westerly phases, while ERA5 shows a significant increase in $\sigma(\omega_{500})$ over the Indian Ocean and Maritime Continent regions during QBO easterly compared to westerly (Fig. 18d), this is not found in the coupled (Fig. 18e) or AMIP (Fig. 18f) simulations.

Since the coupled simulations extend from 1850 to 2100, and prior studies have argued that the QBO-MJO connection may have only appeared in more recent decades as a result of the greenhouse gas influence on the atmospheric temperature structure (Klotzbach et al., 2019), we further assess the difference in $\sigma(\omega_{500})$ between QBO easterly and westerly years in running 45-year segments over the entire simulation length to determine whether there is any growth in the signal as the greenhouse gas forced signal increases, or whether there are any 45-year segments that, by chance, exhibit as big of a signal as seen in reanalyses. Figures 18g and h make it clear that there are no 45-year segments in the simulations that produce as large of a difference between QBO easterly and westerly as seen in the reanalyses and there are no systematic variations in the strength of this difference over time. It is clear, therefore, that despite this model now having an improved representation of the QBO, the relationship between the QBO and MJO activity is still absent.

Randall et al. (2023) recently argued that the QBO-MJO connection may arise through a connection with tropical SSTs given that in the observational record there is a prevalence of La Niña conditions in easterly QBO years compared to westerly years. They ran some simulations with prescribed SSTs that were representative of observed QBO easterly and westerly years and suggested there may be slightly more MJO activity during QBO easterly years as a result of those SSTs. We can use our AMIP simulations to also check for this potential pathway by compositing years based on the *observed* QBO as opposed to the modelled QBO to look at the composite difference in MJO activity between those years that have the same SSTs as in observed QBO easterly and westerly years. While there is clearly La Niña-like conditions in the observed QBO easterly years compared to westerly years (supplemental Fig. S10a), there is no evidence of this having a significant impact on MJO activity (supplemental Figs. S10b and c).

7 Conclusions

CAM7 will have enhanced vertical resolution and the "workhorse" version will have a raised model lid compared to its predecessors. Here, we have presented a series of simulations that informed the decision regarding this enhanced resolution and used them to demonstrate the impacts of vertical resolution on the QBO and other features of the tropical atmosphere. As vertical resolution in the free troposphere and lower stratosphere is increased, the role of the resolved Kelvin waves in driving the QBO is enhanced, as are the amplitudes of equatorial Kelvin waves in the lower stratosphere. The QBO amplitude in the lower stratosphere is increased, but associated with this is also an increase in barotropically unstable states and an increase in MRG activity generated through this instability, associated with a narrow QBO westerly jet. This is not seen to the same degree in reanalyses. Overall, the improvements in the role of the resolved waves in driving the QBO motivated a choice of vertical grid spacing of 500 m throughout the free troposphere and lower stratosphere, aligned with the previous conclusions of Garcia and Richter (2019). For basic features of the stratospheric circulation, a model lid at approximately 80 km was found to produce a similar representation to the 140-km lid WACCM configuration, motivating an overall choice of a raising of CAM's model lid to 80 km. Despite the enhancements in the representation of the QBO that come with this new grid, the series of coupled and AMIP simulations described here do not capture the observed QBO-MJO connection. These simulations are now freely available to anyone who wishes to use them to explore climate variability and change in the presence of a relatively well resolved stratosphere.

The final grids for CAM7 described in section 5 will also include enhanced resolution between the surface and around 700 hPa and a lowering of the lowest model level.

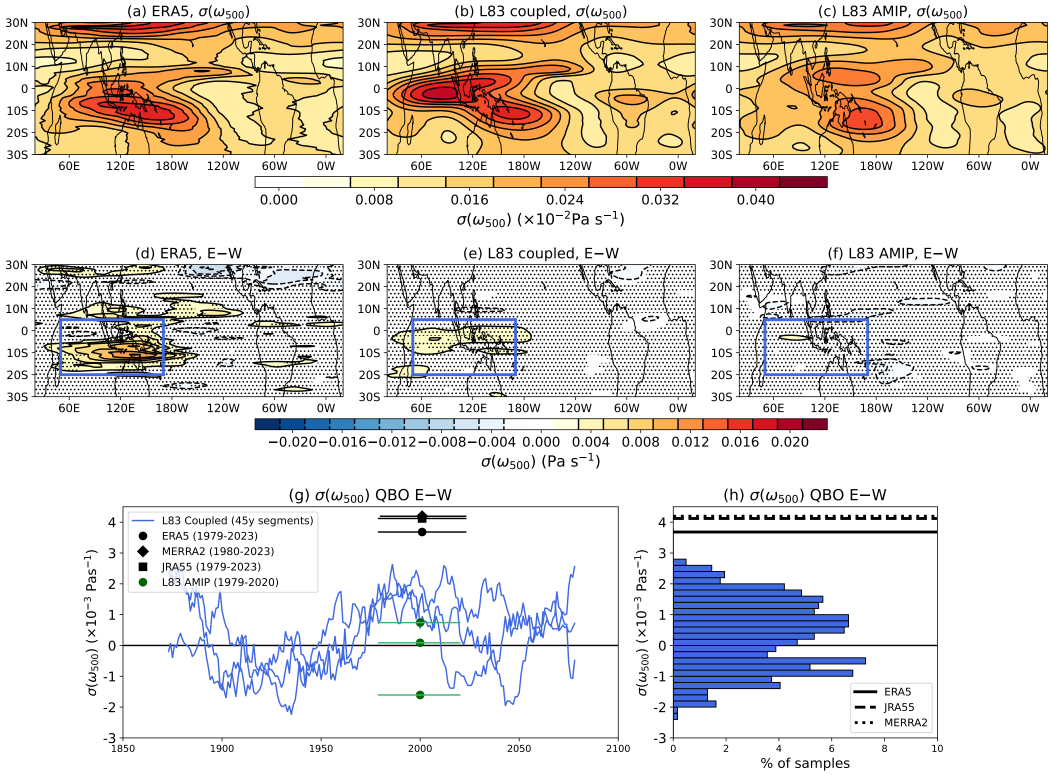

Figure 18. The QBO-MJO connection using MJO-filtered 500-hPa vertical velocity variability during DJF. (a)-(c) the climatological average standard deviation of the MJO-filtered vertical velocity ($\sigma(\omega_{500})$), computed as the standard deviation across days within the winter for each year and then averaged across years for (a) ERA5 from 1979 to 2023, (b) Coupled L83 from 1979 to 2023, and (c) AMIP L83 from 1979 to 2020. (d)-(f) are as (a)-(c) but for the difference in $\sigma(\omega_{500})$ between QBO easterly years and QBO westerly years. Stippling shows regions where the composite difference is not statistically significant at the 95% level by a boostrapping test where the QBO easterly and westerly years from the three members are pooled together and then resampled with replacement 1000 times to produce 1000 QBO easterly minus westerly composites with the same sample size as the original. (g) shows the difference in $\sigma(\omega_{500})$ between easterly and westerly QBO averaged over the blue box in panels (d)-(f), i.e., 50°E to 170°E, 20°S to 5°N. The blue lines show the values obtained using consecutive 45-year windows from 1850 to 2100, i.e., the same length as the 1979 to 2023 ERA5 record. The green points show the L83 AMIP simulations using the period 1979 to 2020 and the black points show the reanalyses over 1979 to 2023, with the horizontal line denoting the time range used in the computation. (h) Shows the PDF of the difference in $\sigma(\omega_{500})$ between QBO easterly and westerly years for all the 45-year segments shown in panel (g) along with the three reanalyses.

We have not incorporated additional lower tropospheric levels into the analysis presented here because doing so would necessarily involve updates and re-tuning of the physical parameterizations and would, therefore, not allow for a clean examination of the impact of vertical resolution. Ultimately, once these additions to the boundary layer are incorporated, a "mid-top" configuration with 93 levels and a model lid at approximately 80 km and a cheaper "low-top" option with 58 levels and a model lid at around 40 km will each be available in CAM7, noting that all else being equal, computational expense scales approximately linearly with resolution. In the troposphere, the resolutions of these two grids will be the same in order to avoid tuning two separate configurations.

Open Research Section

The simulations using the L83 configuration are available for download from https://www.cesm.ucar.edu/working-groups/climate/simulations/cesm2-83level and this dataset has an associatd DOI:10.5065/S125-CA92. The CESM2 large ensemble is available for download from https://www.cesm.ucar.edu/community-projects/lens2 and the CMIP6 WACCM simulations are available for download from the CMIP6 data portal https://aims2.llnl.gov/search/cmip6/. ERA5 is available to download from https://www.ecmwf.int/en/forecasts/datasets/reanalysis-datasets/era5, MERRA2 from https://disc.gsfc.nasa.gov/datasets?project=MERRA-2 and JRA55 from http://jra.kishou.go.jp/JRA-55/index_en.html. The SWOOSH water vapor dataset is available from https://csl.noaa.gov/groups/csl8/swoosh/. In addition, we will make all data available that is required to reproduce the figures of the manuscript on NCAR's Geoscientific Data Exchange once the manuscript has undergone its first round of review.

All analysis codes are available here: https://github.com/islasimpson/CAM7_vertres_paper.

Acknowledgments

This work was supposed by the NSF National Center for Atmospheric Research, which is a major facility sponsored by the NSF under Cooperative Agreement No. 1852977. BM was supported by the U.S. Department of Energy, Office of Science, Office of Biological & Environmental Research (BER), Regional and Global Model Analysis (RGMA) component of the Earth and Environmental System Modeling Program under Award Number DE-SC0022070 and National Science Foundation (NSF) IA 1947282.

References

Abhik, S., & Hendon, H. H. (2019). Influence of the QBO on the MJO During Coupled Model Multiweek Forecasts. *Geophys. Res. Lett.*, *46*, 9213–9221.

Alexander, M. J., & Ortland, D. A. (2010). Equatorial waves in High Resolution Dynamics Limb Sounder (HIRDLS) data. *J. Geophys. Res.*, *115*, D24111.

Andrews, M. B., Knight, J. R., Scaife, A. A., & Wicker, W. (2023). Influence of the Quasi-Biennial Oscillation on tropical convection and its teleconnection to the midlatitudes in boreal winter. *Q. J. Roy. Met. Soc.*, *150*, 2510-2521.

Anstey, J. A., Scinocca, J. F., & Keller, M. (2016). Simulating the QBO in an Atmospheric General Circulation Model; Sensitivity to Resolved and Parameterized Forcings. *J. Atmos. Sci.*, *73*, 1649–1665.

Anstey, J. A., & Shepherd, T. G. (2014). High-latitude influence of the quasi-biennial oscillation. *Quart. J. Roy. Met. Soc.*, *140*, 1-21.

Baldwin, M. P., & Dunkerton, T. J. (2001). Stratospheric Harbingers of Anomalous Weather Regimes. *Science*, *294*, 581.

Baldwin, M. P., Gray, L. J., Dunkerton, T. J., Hamilton, J., Haynes, P. H., Randel, W. J., … Takahashi, M. (2001). The Quasi-Biennial Oscillation. *Rev. Geophys.*, *39*, 179-229.

Bogenschutz, P. A., Yamaguschi, T., & Lee, H.-H. (2023). The Energey Exascale Earth System Model simulations with high vertical resolution in the lower troposphere. *J. Adv. Mod. Earth Sys.*, *13*, e2020MS002239. doi: 10.1029/2020MS002239

Boville, B. A., & Randel, W. G. (1992). Equatorial Waves in a Stratospheric GCM: Effects of Vertical Resolution. *J. Atmos. Sci.*, *49*, 785–801.

Bramberger, M., Alexander, M. J., Davis, S., Podglajen, A., Herzog, A., Kalnajs, L., … Khaykin, S. (2021). First Super-Pressure Balloon-Borne Fine-Versital-Scale Profiles in the Upper TTL: Impacts of Atmospheric Waves on Cirrus Clouds and the QBO. *Geophys. Res. Lett.*, *49*, e2021GL097596.

Bushell, A. C., Anstey, J. A., Butchard, N., Kawatani, Y., Osprey, S. M., Richter, J. H., … Yukimoto, S. (2020). Evaluation of the Quasi-Biennial Oscillation in global climate models for the SPARC QBO-initiative. *Q. J. Roy. Met. Soc.*, *148*, 1459–1489.

Byrkjedal, Ø., Esau, I., & Kvamstø, N. G. (2008). Sensitivity of simulated wintertime Arctic atmosphere to vertical resolution in the ARPEGE/IFS model. *Clim. Dyn.*, *30*, 687–701.

Danabasoglu, G., Lamarque, J.-F., Bacmeister, J., Bailey, D. A., DuVivie r, A. K., Edwards, J., … Strand, W. G. (2020). The Community Earth System Model 2 (CESM2). *J. Adv. Mod. Earth Sys.*, *12*. doi: 10.1029/2019MS001916

Davis, S. M., Rosenlof, K. H., Hassler, B., Hurst, D. F., Read, W. G., Vömel, H., … Damadeo, R. (2016). The Stratospheric Water and Ozone Satellite Homogenized (SWOOSH) database: A long-term database for climate studies. *Earth System Science Data*, *8*, 461–490.

Dessler, A. E., Schoeberl, M. R., Wang, T., Davis, S. M., Rosenlog, K. H., & Vernier, J.-F. (2014). Variations of stratospheric water vapor over the past three decades. *J. Geophys. Res. Atm.*, *119*, 12588-12598.

Domeisen, D. I. V., Butler, A. H., Charlton-Perez, A. J., Ayarzaguena, B., Baldwin, M. P., Dunn-Sigouin, E., … Taguchi, M. (2020). The role of the stratosphere in subseasonal to seasonal prediction: 2. predictability arising from stratosphere-troposphere coupling. *J. Geophys. Res. Atm.*, *125*, e2019JD030923.

Dunkerton, T. J., & Delisi, D. P. (1985). Climatology of the Equatorial Lower Stratosphere. *J. Atmos. Sci.*, *42*, 376–396.

Ern, M., Ploeger, F., Preusse, P., Gille, J. C., Kalisch, S., Mlynczak, M. G., … Riese, M. (2014). Interaction of gravity waves with the QBO: A satellite perspective. *J. Geophys. Res. Atm.*, *119*, 2329–2355.

Ern, M., & Preusse, P. (2009). Wave fluxes of equatorial Kelvin waves and QBO zonal wind forcing derived from SABER and ECMWF temperature space-time spectra. *Atmos. Chem. Phys.*, *9*, 3957–3986.

Eyring, V., Bony, S., Meehl, G., Senior, C. A., Stevens, B., Stouffer, R. J., & Taylor, K. E. (2016). Overview of the Coupled Model Intercomparison Project Phase 6 (CMIP6) experimental design and organization. *Geoscientific Model Development*, *9*, 1937-1958.

Garcia, R. R., & Richter, J. H. (2019). On the Momentum Budget of the Quasi-Biennial Oscillation in the Whole Atmosphere Community Climate Model. *J. Atmos. Sci.*, *76*, 69–87.

Gelaro, R., McCarty, W., Suárez, M. J., Todling, R., Molod, A., Takacs, L., ... Zhao, B. (2017). The Modern-Era Retrospective Analysis for Research and Applications, Version 2 (MERRA-2). *J. Clim.*, *30*, 5419–5454.

Gerber, E., & Manzini, E. (2016). The Dynamics and Variability Model Intercomparison Project (DynVarMIP) for CMIP6: assessing the stratosphere-troposphere system. *Geosci. Mod. Dev.*, *9*, 3413-3425.

Gettelman, A., Mills, M. J., Kinnison, D. E., Garcia, R. R., Smith, A. K., Marsh, D. R., ... Randel, W. G. (2019). The Whole Atmosphere Community Climate Model Version 6 (WACCM6). *J. Geophys. Res. Atm.*, *124*. doi: 10.1029/2019JD030943

Giorgetta, M. A., Manzini, E., & Roeckner, E. (2002). Forcing of the quasi-biennial oscillation from a broad spectrum of atmospheric waves. *Geophys. Res. Lett.*, *29*. doi: 10.1029/2001GL014756

Giorgetta, M. A., Manzini, E., Roeckner, E., Esch, M., & Bengtsson, L. (2006). Climatology and Forcing of the Quasi-Biennial Oscillation in the MAECHAM5 Model. *J. CLim.*, *19*, 3882–3901.

Hayashi, Y. (1971). A generalized method of resolving disturbances into progressive and retrogressive waves by space Fourier and time cross-spectral analysis. *J. Meteor. Soc. Japan.*, *49*, 125-128.

Hersbach, H., Bell, B., Berrisford, P., Hirahara, S., Horányi, A., Muñoz-Sabater, J., ... Thépaut, J.-N. (2020). The era5 global reanalysis. *Quarterly Journal of the Royal Meteorological Society*, *146*(730), 1999-2049. doi: https://doi.org/10.1002/qj.3803

Hitchcock, P., & Simpson, I. R. (2014). The Downward Influence of Stratospheric Sudden Warmings. *J. Atmos. Sci.*, *71*, 3856–3876.

Holt, L. A., Alexander, M. J., Coy, L., Molod, A., Putman, W., & Pawson, S. (2016). Tropical Waves and the Quasi-Biennial Oscillation in a 7-km Global Climate Simulation. *J. Atmos. Sci.*, *73*, 3771-3783.

Holt, L. A., Lott, F., Garcia, R. R., Kiladis, G. N., Cheng, Y.-M., Anstey, J. A., ... Yukimoto, S. (2021). An evaluation of tropical waves and wave forcing of the QBO in the QBOi models. *Q. J. Roy. Met. Soc*, *148*, 1541–1567.

Holton, J. R., & Lindzen, R. S. (1972). An Updated Theory for the Quasi-Biennial Cycle of the Tropical Stratosphere. *J. Atmos. Sci.*, *29*, 1076–1080.

Huang, B., Thorne, P. W., Banzon, V. F., Boyer, T., Chepurin, G., Lawrimore, J. H., ... Zhang, H.-M. (2017). Extended Reconstructed Sea Surface Temperature, Version 5 (ERSSTv5): Upgrades, Valifations, and Intercomparisons. *J. Clim.*, *30*, 8179–8205.

Hurrell, J. W., Hack, J. J., Shea, D., Caron, J. M., & Rosinski, J. (2008). A New Sea Surface Temperature and Sea Ice Boundary Dataset for the Community Atmosphere Model. *Notes and Correspondence*, *21*, 5145-5153.

Hurrell, J. W., Holland, M. M., Gent, P. R., Ghan, S., Kay, J. E., Kushner, P. J., ... Marshall, S. (2013). The Community Earth System Model: A Framework for Collaborative Research. *Bull. Amer. Meteor. Soc.*, *94*, 1339-1360.

Jiang, L., & Hu, J. (2023). Influence of the lowest model level height and vertical grid resolution on mesoscale meteorological modeling. *Atmospheric Research*, *296*, 107066. doi: 10.1016/j.atmosres.2023.107066

Kawatani, Y., Sato, K., Dunkerton, T. J., Watanabe, S., Miyahara, S., & Takahashi, M. (2010). The Roles of Equatorial Waves and Internal Inertia-Gravity Waves in Driving the Quasi-Biennial Oscilaltion. Part 1: Zonal Mean Wave Forcing. *J. Atmos. Sci.*, *67*, 963–980.

Kay, J. E., Deser, C., Phillips, A., Mai, A., Hannay, C., Strand, G., … Vertenstein, M. (2014). The Community Earth System Model (CESM) Large Ensemble Project. *Bull. Amer. Meteor. Soc.*, *96*, 1333–1349.

Kim, H., Caron, J. M., Richter, J. H., & Simpson, I. R. (2020). The Lack of QBO-MJO Connection in CMIP6 Models. *Geophys. Res. Lett.*, *47*, e2020GL087295. doi: 10.1029/2020GL087295

Kim, H., Richter, J. H., & Martin, Z. (2019). Insignificant QBO-MJO prediction skill relationship in the SubX and S2S subseasonal reforecasts. *J. Geophys. Res.: Atmospheres*, *124*, 12655–12666.

Kim, Y.-H., & Chun, H.-Y. (2015). Momentum forcing of the quasi-biennial oscillation by equatorial waves in recent reanalyses. *Atmos. Chem. Phys.*, *15*, 6577–6587.

Klotzbach, P., Abhik, S., Hendon, H. H., Bell, M., Lucas, C., Marshall, A. G., & Oliver, E. C. J. (2019). On the emerging relationship between the stratospheric Quasi-Biennial Oscillation and the Madden-Julian Oscillation. *Scientific Reports*, *9*, 2981.

Kobayashi, S., Ota, Y., Harada, Y., Ebita, A., Moriya, M., Onoda, H., … Takahashi, K. (2015). The jra-55 reanalysis: General specifications and basic characteristics. *J. Met. Soc. Japan.*, *93*, 5–48.

Lauritzen, P. H., Nair, R. D., Herrington, A. R., Callaghan, P., Goldhaber, S., Dennis, J. M., … Trippia, J. J. (2018). Spectral Element Dynamical Core in Dry-Mass Vertical Coordinates With Comprehensive Treatment of Condensates and Energy. *J. Adv. Mod. Earth Sys.*, *10*, 1537–1570.

Lee, H.-K., Chun, H.-Y., Richter, J. H., Simpson, I. R., & Garcia, R. R. (2024). Contributions of Parameterized Gravity Waves and Resolved Equatorial Waves to the QBO Period in a Future Climate of CESM2. *J. Geophys. Res.*, *129*, e2024JD040744. doi: 10.1029/2024JD040744

Lee, J. C. K., & Klingaman, N. P. (2018). The effect of the quasi-biennial oscillation on the Madden-Julian oscillation in the Met Office Unified Model Global Ocean Mixed Layer configuration. *Atmospheric Science Letters*, *19*, e816. doi: 10.1002/asl.816

Li, W. J. L. J.-J. Y. Y. M., Y. (2022). Evaluating the Eastward Propagation of the MJO in CMIP5 and CMIP6 Models Based on a Variety of Diagnostics. *J. Clim.*, *35*, 1719–1743.

Lin, S. J. (2004). A "vertically Lagrangian" finite-volume dynamical core for global models. *Mon. Weath. Rev.*, *132*, 2293–2307.

Lin, S. J., & Rood, R. B. (1997). An explicit Flux-Form Semi-Lagrangian shallow water model on the sphere. *Q. J. Roy. Met. Soc.*, *123*, 2477–2498.

Martin, Z., Son, S.-W., Butler, A., Hendon, H., Kim, H., Sobel, A., … Zhang, C. (2021). The influence of the quasi-biennial oscillation on the Madden-Julian oscillation. *Nature Reviews: Earth and Environment*, *2*, 477–489.

Martin, Z., Vitart, F., Wang, S., & Sobel, A. (2020b). The Impact of the Stratosphere on the MJO in a Forecast Model. *J. Geophys. Res.: Atmospheres*, *125*, e2019JD032106.

Martin, Z. K., Simpson, I. R., Lin, P., Orbe, C., Tang, Q., Caron, J. M., … Xie, S. (2023). The Lack of a QBO-MJO Connection in Climate Models With a Nudged Stratosphere. *J. Geophys. Res.: Atmospheres*, *128*, e2023JD038722.

McTaggart-Cowan, R., Vaillancourt, P. A., Zadra, A., Chamberland, S., Charron, M., & Corvec, S. (2019). Modernization of atmospheric physics parameterization in Canadian NWP. *J. Adv. Mod. Earth Sys.*, *11*, 3593–3635.

Niemeier, U., Wallis, S., Timmreck, C., van Pham, T., & von Savigny, C. (2023). How the Hunga Tonga-Hunga Ha'apai Water Vapor Cloud Impacts Its Transport Through the Stratosphere: Dynamical and Radiative Effects. *Geophys. Res. Lett.*, *50*, e2023GL106482.

Pahlavan, H. A., Fu, Q., Wallace, J. M., & Kiladis, G. N. (2021). Revisiting the Quasi-Biennial Oscillation as Seen in ERA5 Part 1: Description and Momentum Budget. *J. Atmos. Sci.*, *78*, 673–691.

Pahlavan, H. A., Wallace, J. M., Fu, Q., & Kiladis, G. N. (2021). Revisiting the Quasi-Biennial Oscillation as Seen in ERA5. Part 2: Evaluation of Waves and Wave Forcing. *J. Atmos. Sci.*, *78*, 693–707.

Randall, D. A., Tziperman, E., Branson, M. D., Richter, J. H., & Kang, W. (2023). The QBO-MJO Connection: A Possible Role for the SST and ENSO. *J. Clim.*, *36*, 6515–6531.

Rayner, N. A., Parker, D. E., Horton, E. B., Folland, C. K., Alexander, L. V., Rowell, D. P., … Kalplan, A. (2003). Global analyses of sea surface temperature, sea ice, and night marine air temperature since the late nineteenth century. *J. Geophys. Res.*, *108*, D14.

Reynolds, R. W., Rayner, T. M., Smith, D. C., & Wang, W. (2002). An improved in situ and satellite SST analysis for climate. *J. Clim.*, *15*, 1609–1625.

Ricciardulli, L., & Garcia, R. R. (2000). The Excitation of Equatorial Waves by Deep Convection in the NCAR Community Climate Model (CCM3). *J. Atmos. Sci.*, *57*, 3461–3487.

Richter, J. H., Anstey, J. A., Butchart, N., Kawatani, Y., Meehl, G. A., Osprey, S., & Simpson, I. R. (2020). Progress in Simulating the Quasi-Biennial Oscillation in CMIP Models. *J. Geophys. Res. Atm.*, *125*, e2019JD032362.

Richter, J. H., Glanville, A. A., Edwards, J., Kauffman, B., David, N. A., Jaye, A., … Oleson, K. W. (2022). Subseasonal Earth System Prediction with CESM2. *Weather and Forecasting*, *37*, 797–815.

Richter, J. H., Sassi, F., & Garcia, R. R. (2010). Toward a Physically Based Gravity Wave Source Parameterization in a General Circulation Model. *J. Atmos. Sci.*, *67*, 136-156.

Richter, J. H., Solomon, A., & Bacmeister, J. T. (2014). On the simulation of the quasi-biennial oscillation in the Community Atmosphere Mode, version 5. *J. Geophys. Res. Atm*, *119*, 3045–3062.

Rodgers, K. B., Lee, S.-S., Rosenbloom, N., Timmermann, A., Danabasoglu, G., Deser, C., … Yeager, S. G. (2021). Ubiquity of human-induced changes in climate variability. *Earth Sys. Dynam.*, *12*, 1393-1411.

Shaw, T. A., & Shepherd, T. G. (2008). Raising the Roof. *Nat. Geosc.*, *1*, 12–13.

Smith, K. L., Neely, R. R., Marsh, D. R., & Polvani, L. M. (2014). The Specified Chemistry Whole Atmosphere Community Climate Model (SC-WACCM). *J. Adv. Model. Earth Syst.*, *6*, 883–901.

Sudqvist, H., & Veronis, G. (1970). A simple finite-difference grid with non-constant intervals. *Tellus*, *22*, 26-31.

Vincent, R. A., & Alexander, M. J. (2020). Balloon-Borne Observations of Short Vertical Wavelenth Gravity Waves and Interaction With QBO Winds. *J. Geophys. Res. Atm.*, *125*, e2020JD032779.

Wheeler, M., & Kiladis, G. N. (1998). Convectively Coupled Equatorial Waves: Analysis of Clouds nad Temperature in the Wavenumber-Frequency Domain. *J. Atmos. Sci.*, *56*, 374–399.

Yeager, S. G., Rosenbloom, N., Glanville, A. A., Wu, X., Simpson, I., Li, H., … King, T. (2022). The Seasonal-to-Multiyear Large Ensemble (SMYLE) prediction system using the Community Earth System Model version 2. *Geosci. Model Dev.*, *15*, 6451–6493.

Yoo, C., & Son, S.-W. (2016). Modulation of the boreal wintertime Madden-Julian oscillation by the stratospheric quasi-biennial oscillation. *Geophys. Res. Lett.*, *43*, 1392–1398.